

CHARLES UNIVERSITY IN PRAGUE
FACULTY OF SCIENCE
INSTITUTE OF PETROLOGY AND STRUCTURAL GEOLOGY



**Structural evolution and U/Pb dating of the Hammar Domain
(East-African Orogeny)**

Strukturní vývoj a U/Pb datování hammerské jednotky
(východoafrický orogen)

Diploma Thesis

Diplomová práce

Belule Bezuneh Melka, B.Sc.

Supervisor / školitel:

Doc. RNDr. Kryštof Verner, Ph.D.

Prague, May 2023

Acknowledgment

First of all, I would like to thank the ‘Almighty God’ who made it possible to begin and finish the thesis research work successfully after so many challenging times. I sincerely thank the Czech Government for the Development Cooperation Project Program done by the Czech Geological Survey under the supervision Assoc. Prof. Kryštof Verner and his staff for giving me the full scholarship to do this master degree. I am greatly indebted to my employer Geological Survey of Ethiopia (GSE) for allowing me to use this opportunity. My very sincere gratitude to my supervisor Assoc. Prof. Kryštof Verner and Dr. Leta Alemayehu Megerssa for their kindness and recommended me for this chance and facilitate all things starting from the beginning until the completion of my master degree. I would also like to thank to Dr. David Buriánek and Dr. Karel Martínek for their support and guidance. I greatly appreciate and say thank you for all Institute of Petrology and Structural Geology staff as a whole. At last but not the least I would say thanks to my lovely and wonderful parents and siblings for their support and care. Finally, I give all glory and honor to God that made the program possible.

This Master's Thesis was processed in frame of the Czech development cooperation project in Ethiopia entitled "“Ensuring Sustainable Land Management in Selected Areas of Ethiopia on the Basis of Geoscientific Mapping” in the years 2021 to 2023.

Declaration:

I declare that I am author of this diploma thesis and I have cited all resources used in its preparation. Neither this thesis nor its substantial part has been submitted to fulfill requirements for other master or any other academic degree.

Prohlášení:

Prohlašuji, že jsem tuto diplomovou práci vypracoval samostatně a výhradně s použitím citovaných pramenů, literatury a dalších odborných zdrojů. Tato práce ani její podstatná část nebyla předložena k získání jiného nebo stejného akademického titulu.

In Prague, May 15, 2023.

Keywords:

Fabric pattern; U/Pb dating; Hammar Domain; Southern Ethiopian Shield; East-African Orogeny

Abstract in English

Studied parts of the Hammar Domain and Adola-Moyale Belt is situated at the junction of the Arabian Nubian Shield (ANS) and Mozambique Belt (MB) as a crucial area where to study the overall imprint of the East-African Orogeny in Ethiopia.

Based on detailed field geological mapping, morphotectonic analysis of Digital Elevation Model, detailed structural analysis and U/Pb dating results of biotite orthogneiss from the Hammar Domain the overall tectonic evolution associated with the East-African Orogeny is interpreted.

The structural evolution of the northern Hammar Domain and northwestern tip of the Adola-Moyale Belt could be defined into four deformation phases D_1 to D_4 resulted in origin of: (a) Relict compositional banding (S_1) of flat-lying orientation defining the primary contacts of high- to medium grade lithologies, (b) superimposed steeply to moderately dipping $\sim N-S$ to $\sim NW-SE$ trending compressional foliation (S_2) due to a regional $\sim E-W$ oriented compression and (c) later sub-horizontal to gently NW dipping foliation (S_3) associated with well-developed NW plunging lineation. Furthermore, the localized tectonic activity was concentrated in form of narrow brittle-ductile to brittle $\sim N-S$ to $\sim NW-SE$ trending shear zones, commonly accompanied by hydrothermal mineralization.

New geochronological data from biotite orthogneiss yielded at 773.2 ± 5.8 Ma reveal the magmatic (crystallization) age of granite photolith. The rock assemblage has been affected by polyphase deformation and recrystallization due to main collisional event and exhumation at ca. 660 Ma which corresponds to Gondwana continent assembly.

Abstrakt (v českém jazyce)

Studované části hammarské domény a pásu Adola-Moyale se nachází na pomezí Arabsko-núbijského štítu (ANS) a mosambického pásu (MB). Jedná se o důležité oblasti kde lze studovat záznam východoafrických orogenenních procesů v Etiopii. Na základě podrobného terénního geologického mapování, morfotektonické analýzy digitálního modelu reliéfu, strukturní analýzy a výsledků U/Pb datování biotitické ortoruly z hammarské domény byl interpretován celkový tektonický vývoj oblasti spojený s východoafrickou orogenní fází.

Výsledky morfotektonické analýzy digitálního modelu reliéfu reprezentují jak širší spektrum zlomových struktur, které byly aktivní od období neoproterozoika až po současnost, tak i výrazná litologická rozhraní.

Strukturní vývoj severní části hammarské domény a severozápadní části pásu Adola-Moyale lze definovat ve čtyřech deformačních fázích D_1 až D_4 , jehož výsledkem je: (a) tvorba reliktního kompozičního páskování (S_1), které definuje primární litologické kontakty, (b) superponovaná strmě orientovaná kompresní foliace (S_2) s-j. až sz-jv. průběhu, jejíž vznik je důsledkem regionální ~V-Z orientované komprese a (c) superpozice subhorizontální až mírně k ~SZ upadající foliace (S_3) s výraznými lineacemi. Dále, lokalizovaná tektonická aktivita byla koncentrována ve formě úzkých křehko-duktilních až křehkých deformačních zón, které mají strmou orientaci v průběhu S-J až SZ-JV a jsou často doprovázena hydrotermální mineralizací.

Nová geochronologická data z biotitické ortoruly se stářím $773,2 \pm 5,8$ Ma ukazují magmatický (krystalizační) věk granitového protolitu. Hornina dále byla ovlivněna polyfázovou deformací a rekrytalizací v důsledku hlavní kolizní události a exhumace při ca. 660 Ma, což odpovídá hlavní fázi konsolidace kontinentu Gondwana.

Table of Contents

Acknowledgment	i
<i>Abstrakt (v českém jazyce)</i>	iv
1. Introduction	1
2. Geological settings	4
2.1. East African Orogeny (EAO)	4
2.2. The study areas in the Southern Ethiopian Shield (SES)	12
3. Methodology	17
3.3. U-Pb dating.....	20
4. Morphotectonic analysis	21
5. Lithology	24
5.1. Northern Hammar Domain of Gamo Zone (Neoproterozoic basement rocks)	25
5.2. Northwestern Adola-Moyale Belt of Sidama Region (Neoproterozoic rocks)	27
5.3. Cenozoic volcano-sedimentary sequences of the Main Ethiopian Rift.....	30
6. Tectonics.....	33
6.1. Neoproterozoic rocks of the Hammar Domain and Adola-Moyale Belt.....	33
6.2. Fabric pattern in overlying volcanic rocks and volcanoclastic deposits (MER)	39
6.3. Brittle Structures.....	41
7. U-Pb Dating.....	43
8. Geological map compilation.....	44
9. Discussion.....	45
10. Conclusions	47
<i>List of References:</i>	48
<i>Annexes</i>	51

List of Figures

<i>Figure 1. The location map of study area..</i>	<i>3</i>
<i>Figure 2. Reconstruction of the East African Orogen..</i>	<i>4</i>
<i>Figure 3. Two-dimensional summary of the tectonic evolution of the East African Orogen</i>	<i>5</i>
<i>Figure 4. Historic Overview the Arabian–Nubian Shield (Peter R. Johnson, 2021)..</i>	<i>8</i>
<i>Figure 5. Sketch of Gondwana supercontinent assembly and position of ANS.</i>	<i>11</i>
<i>Figure 6. Scenario of geodynamic evolution of the Hammar Domain (Southern Ethiopian Shield) in the context of East-African Orogeny.</i>	<i>16</i>
<i>Figure 7. Principal Component Analysis (PCA) transform of the Sentinel–2 imagery of the Gamo Zone..</i>	<i>18</i>
<i>Figure 8. Principal Component Analysis (PCA) transform of the Sentinel–2 imagery of Sidama Region.....</i>	<i>19</i>
<i>Figure 9. Digital elevation models (DEM) of the Gamo Zone with interpretation of morphotectonic linear indices</i>	<i>22</i>
<i>Figure 10. Rose diagram showing the orientation frequency of linear indices (morpholineaments).</i>	<i>22</i>
<i>Figure 11. Digital elevation models (DEM) of the Sidama Region.</i>	<i>23</i>
<i>Figure 12. Schematic sketch of the Southern Ethiopian Shield (SES) and position of both studied areas.</i>	<i>24</i>
<i>Figure 13. Simplified sketch the Gamo Zone including the main lithotectonic units and the extent of the studied area.</i>	<i>25</i>
<i>Figure 14. Field photograph of medium-grained biotite orthogneiss.</i>	<i>26</i>
<i>Figure 15. Field photograph of amphibolite.....</i>	<i>26</i>
<i>Figure 16. Regional simplified geological schematic map of the Sidama Region.....</i>	<i>27</i>
<i>Figure 17. Field photograph of biotite to muscovite-biotite paragneiss</i>	<i>28</i>
<i>Figure 18. Field photograph of medium-grained foliated biotite orthogneiss.</i>	<i>28</i>
<i>Figure 19. Field photograph of banded amphibolite with isoclinal folds of leucosome</i>	<i>29</i>
<i>Figure 20. The field photograph of highly altered trachyte to trachybasalt.....</i>	<i>31</i>

<i>Figure 21. The field photograph of basalt to trachybasalt lava with subordinate basaltic pyroclastic deposits (called as the Amaro-Gamo basalt; Stewart and Rogers, 1996).....</i>	<i>31</i>
<i>Figure 22. Schematic structural map of the southernmost part of the Hammar Domain and overlying volcanic and volcanoclastic sequences of the Main Ethiopian Rift.....</i>	<i>34</i>
<i>Figure 23. Outcrops of rift-related volcanic or volcanoclastic rocks overlying the sequences of metamorphic rocks of the Hammar Unit.....</i>	<i>35</i>
<i>Figure 24. Orientation diagrams (equal projection to the lower hemisphere).....</i>	<i>36</i>
<i>Figure 25. Mesoscopic photographs of metamorphic foliation.....</i>	<i>36</i>
<i>Figure 26. Mesoscopic photographs of magma mingling (MME).....</i>	<i>36</i>
<i>Figure 27. Simplified tectonic map of the Sidama Region showing a regional fabric pattern and mapped faults.....</i>	<i>37</i>
<i>Figure 28. Younger foliation S_3 in biotite orthogneisses.....</i>	<i>38</i>
<i>Figure 29. Quartz vein with discordant contacts.....</i>	<i>38</i>
<i>Figure 30. Orientation diagrams of metamorphic foliation and mineral lineation.....</i>	<i>38</i>
<i>Figure 31. Equal projection to the lower hemisphere diagram and schematic block diagram of hydrothermal quartz vein and regional N-S trending shear zone.....</i>	<i>39</i>
<i>Figure 32. Orientation diagrams of the primary structures in volcanic and volcanoclastic sequences.....</i>	<i>40</i>
<i>Figure 33. Field photo of Early-rift basalt lava flow with well-developed columnar jointing (upper part) overlying ash-fall pyroclastic deposits and Bedding plane.....</i>	<i>40</i>
<i>Figure 34. N–S trending rift-related faults in medium-grade rocks of the Hammar Domain.....</i>	<i>41</i>
<i>Figure 35. Orientation diagrams of faults / fault zones in southern Gamo zone and southeastern Sidama Region overlying volcanites of Main Ethiopian Rift.....</i>	<i>41</i>
<i>Figure 36. Orientation diagrams of extensional joints in southern Gamo zone and southeastern Sidama Region overlying volcanites of Main Ethiopian Rift.....</i>	<i>42</i>
<i>Figure 37. Concordia plot diagram of U/Pb dating.....</i>	<i>43</i>

1. Introduction

The East African Orogen (EAO) is one of Earth's great deformation belts, stretching N–S along the eastern flank of Africa which resulted from the collision of two Neoproterozoic continental masses, the East Gondwana (India–Australia–Antarctica) and the West Gondwana (Africa–South America). These continental collisions first led to crustal thickening and uplift, and continued with escape tectonics until the end of the Precambrian (Stern, 1994). The EAO consists of deformed and metamorphosed rocks of the Arabian Nubian Shield (ANS) in the north and high-grade metamorphism with more strongly deformed rock assemblage in the southern segment, designated as the Mozambique Belt (MB).

The ANS region underwent uplift in relation to the Cenozoic plume related regional flood basalt eruption and subsequent east African rift development around the Red Sea, exposing a large tract of mostly juvenile Neoproterozoic crust (Kroner et al. 2004). The ANS is an accretionary terrane of juvenile material (volcanic and volcano-sedimentary rocks) with dominantly subduction-related magmatism (Asrat et al. 2001; Fritz et al. 2013). The MB on the other hand is a Neoproterozoic, polycyclic, collisional belt that extends along and underlies the eastern margin of much of the African continent (Shackleton 1979) juxtaposing to the south of the ANS. The MB involved more recycling of older crustal material (gneisses and migmatites) and dominantly post collisional magmatism (Asrat et al. 2001).

In Ethiopia Proterozoic terrains belonging to the EAO are partly overlaid by Phanerozoic volcano-sedimentary sequences and exposed in separated windows along the northern, western, southern, and eastern peripheries as shields (Asrat et al. 2000; Fritz et al. 2013). The Western Ethiopian Shield (WES) developed following the Tulu Dimtu Orogenic Belt which is formed during the amalgamation of western Gondwana before the final closure of the Mozambique Ocean (Allen and Tadesse, 2003). WES is situated at the key location of the transition between the Arabian Nubian Shield to the north and the Mozambique Belt to the south (Tadesse and Allen, 2005; Blades et al. 2017). The tectonic evolution of the southern ANS through a Wilson Cycle is well illustrated in the Tulu Dimtu belt of central Ethiopia (Johnson and Woldehaimanot, 2003; Tadesse and Allen, 2005; Woldemichael et al. 2010). Accordingly, early rifting was initiated between 900 and 860 Ma and then the transition from rifting to ocean floor spreading occurred between 860 and 830 Ma followed by the subduction

and formation of arc- and back-arc basins occurred between 830 and 750 Ma; and finally, basin closure by accretion of island arcs commenced between 750 and 650 Ma (Woldemichael et al. 2010 and references therein). U–Pb zircon geochronological studies suggested that the Precambrian, southern ANS in Ethiopia is dominated by granitoids and orthogneisses emplaced between 900 and 550 Ma (Teklay et al. 1998; Yibas et al., 2000; Asrat and Barbey, 2003; Stern et al., 2013).

The Southern Ethiopian Shield (SES) is situated at the junction of the ANS and MB that has a juvenile origin far away from cratonic sources derived from a volcano-sedimentary intra-oceanic magmatic arc of early EAO, ca. 770 Ma (Worku and Schandelmeier, 1996; Verner et al. 2021). Two domains can be identified from the fragmental literature dealing with the metamorphic belts in the southern Ethiopia as the Adola-Moyale (Worku and Schandelmeier, 1996; Yihunie et al., 2004; Tsige and Abdelsalam, 2005) and the Hammar-Surma-Akobo (Davidson 1983; Gichile 1992; Asrat et al. 2003). The Adola-Moyale Domain is comprised of granite-gneiss basement interleaved with three belts (Megado, Kenticha, and Bulbul) of greenschist-facies metamorphic rock assemblages that originated from ophiolites and volcanosediments (Worku and Schandelmeier, 1996; Yibas et al., 2002). The Adola-Moyale belt has been described as a positive flower structure (Tolessa et al. 1991; Ghebreab, 1992) suggesting that the southern ANS developed as a transcurrent orogen with an oblique NW–SE to NE–SW directed shortening components (e.g. Worku and Schandelmeier, 1996). Hammar Domain corresponds to the area in between the western and southern metamorphic terrain of Ethiopia. It is comprised of two major rock groups that differ in the lithological and the mineralogical compositions along with granitic and other intrusive (Davidson, 1983). The Hammar Domain reflects similar geodynamic evolution to the Adola-Moyale Belt which can be summarized into four phases of deformational events (Verner et al. 2021).

This work was done with the cooperative between Czech Geological Survey and Geological Survey of Ethiopia starting from 2018 until now under an umbrella of project. The field work and the subsequent compilation of the geological map as well the structural analysis took place in cooperation with the solution of the Czech Development Cooperation project in the years 2020 to 2022. The partial results obtained as part of this work are part of the compilation work from the Sidama region (Verner et al. 2022) and Gamo zones (Verner et al. in preparation).

The main objective of the thesis is to derive the implication of the tectonometamorphic records tandem with their timing in the Hammar Domain and the Adola-Moyale Domain with respect to the currently accepted geodynamic evolution of the southern Ethiopian Shield during the East African Orogeny. These areas are located in the Sidama Region corresponding to the Adola-Moyale Domain and the Gamo Zone corresponding to the Hammar Domain (Fig. 1). Based on detailed geological mapping, field structural analysis, morphotectonic interpretation of remote sensing data, and U-Pb dating of medium to high-grade metamorphic rocks from the studied areas, a comprehensive understanding of the geodynamic evolution reflected in the areas is drawn.

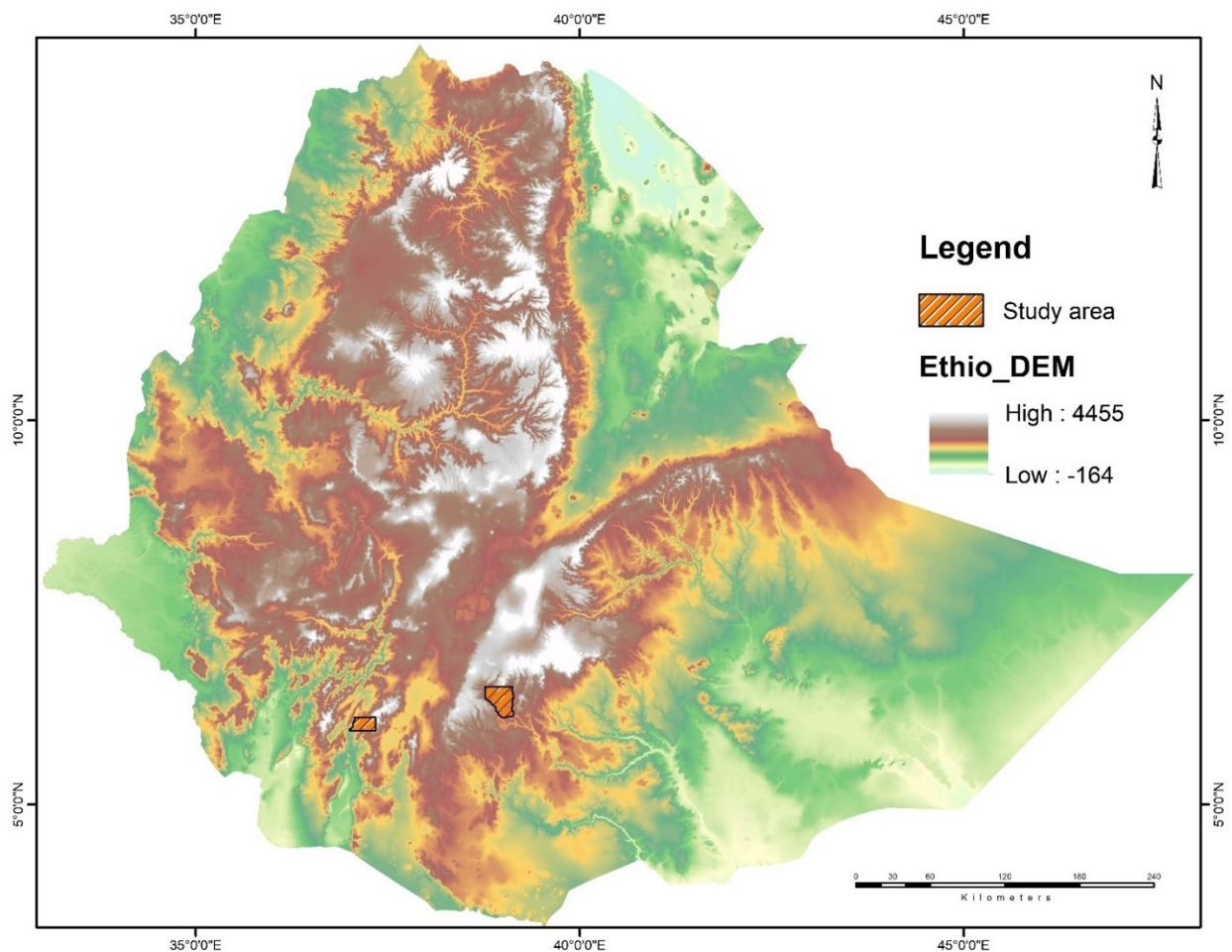


Figure 1. The location map of study area. Left side shaded area is Southwestern Gamo Zone and right-side shaded area represent southeastern of Sidama Region.

2. Geological settings

2.1. East African Orogeny (EAO)

The East African Orogen (EAO) was formed at the helm of formation of the Gondwana continent between 650 and 600 Ma as one of the largest accretionary orogens (Stern 1994; Collins and Pisarevsky 2005; Squire 2006; Fritz et al. 2013). The evolution reflects a Neoproterozoic-Cambrian Wilson Cycle that began with the breakup of Rodinia (870–800 Ma; Kusky et al., 2003; Li et al., 2008) and led to the final amalgamation of Gondwana in Cambrian time. The EAO evolved from the collision of two Neoproterozoic continental masses, the East Gondwana (India–Australia–Antarctica) and the less defined West Gondwana (Africa–South America) (Meert 2003). This collision left an oceanic free-face in the north leading to the escape of the resulting Arabian–Nubian Shield in the norther segment of the EAO toward this free-board leading to the formation of rifted basins in NE Africa and Arabia during the late-Neoproterozoic time (Bonavia and Chorowicz 1993, 1992). The EAO involved accretion of magmatic arc terranes in the ANS between the Sahara Meta-craton and the Congo–Tanzania

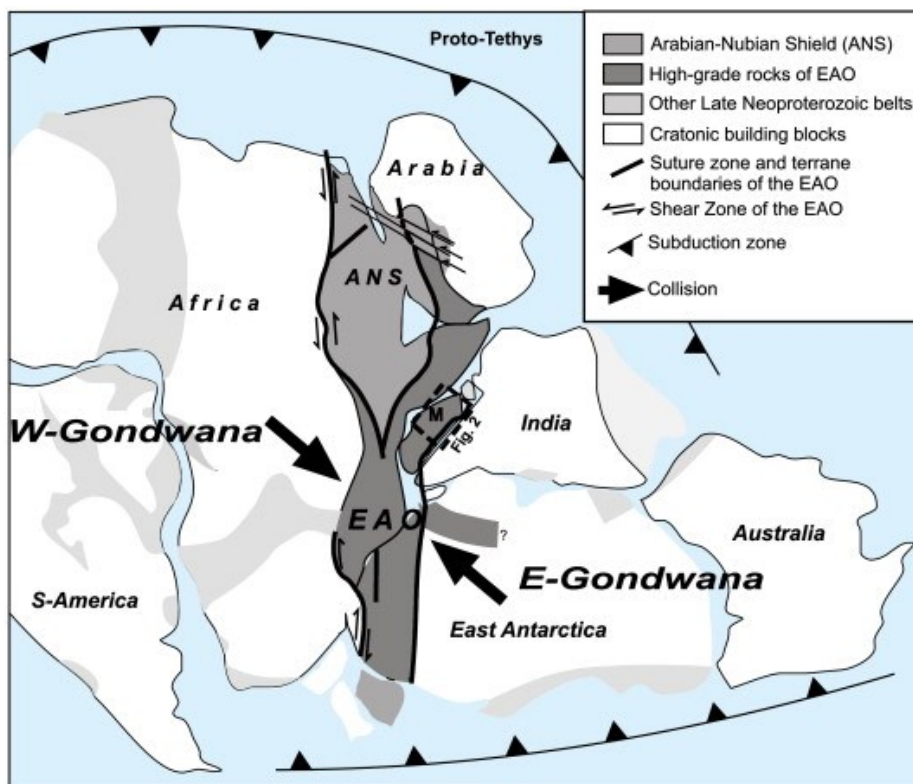


Figure 2.
Reconstruction of
the East African
Orogen.
(According to
Goodenough et al.,
2010).

Cratons to the west and the Azania and Afif terranes to the east (Stern 1994; Fritz et al., 2013). It constitutes one or more continental blocks between the Indian Shield and Congo–Tanzania–Bangweulu Craton (Fritz et al., 2013 and references therein). The continental collision first led to crustal thickening and uplift, followed by escape tectonics until the end of Precambrian. EAO is one of Earth’s great deformation belts, stretching N–S along the eastern flank of Africa (Stern et al., 2012, Fritz et al., 2013). Crust-forming process and plate tectonics indicates the presence of oceanic and continental margin arcs currently recognized in the Neoproterozoic rocks of the Arabian-Nubian shield and Mozambique Belt (de Wit and Sembedo 1981; Vail 1985; Shackleton 1986; Kroner et al. 1987). The EAO segments were intruded by Neoproterozoic and Early Paleozoic plutons from ~880 to ~500 Ma (Johnson et al., 2011; Stern et al. 2012). These igneous bodies and their metamorphosed equivalents give radiometric ages and chemical compositions that can be used to infer tectonic evolution of the EAO. The Neoproterozoic evolution of ANS was punctuated by multiple tectonometamorphic and igneous cycles of which most significant are development of island arcs, their accretion and finally juxtaposition to the cratons (Abdelsalam and Stern, 1996; Johnson and Woldehaimanot, 2003). The subsequent tectonometamorphic phase followed a period of reduced igneous activity (around 700 Ma; Avigad et al., 2007; Meert, 2003), during thickening of the accreted island-arc complexes and formation of tight, roughly N–S striking, upright fold and thrust belts.

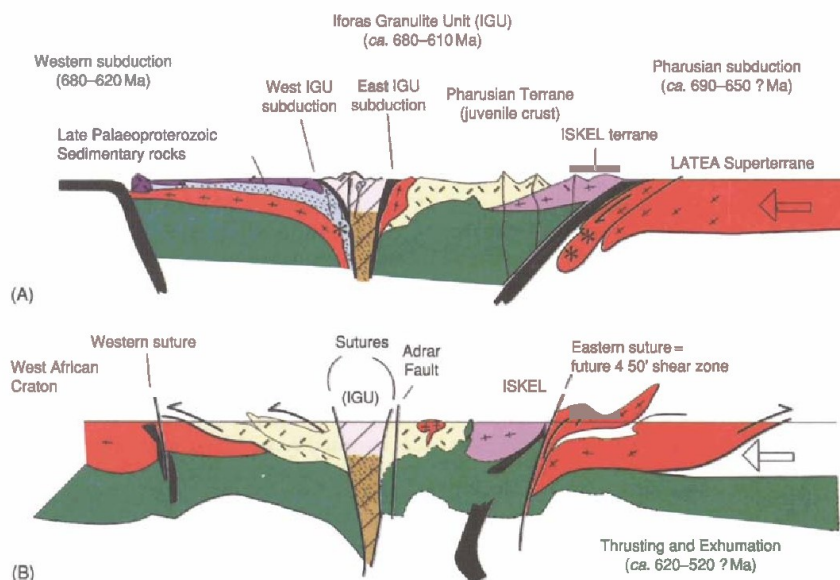


Figure 3. Two-dimensional summary of the tectonic evolution of the East African Orogen (After Stern, 1994).

Mozambique Belt (MB)

The Mozambique Belt (MB) is a Neoproterozoic, polycyclic, collisional belt in the southern EAO that extends along and underlies the eastern margin of the African continent (Shackleton 1979; Fritz et al. 2013). This broad belt defines the southern segment of the EAO extending south from the Arabian-Nubian Shield into southern Ethiopia, Kenya and Somalia through Tanzania, Malawi, and Mozambique including Madagascar (Fritz et al. 2013). The southwestern Ethiopia falls in the Tokar-Barka and Baragoi terranes of the ANS surrounded by the Nakasib suture zone in the north, and the Nyangere and Mutitio shear zones in the south. These terranes are partly overlaid by Phanerozoic volcano-sedimentary sequences and exposed in separated basement shields as the Northern (NES), Western (WES), Southern (SES) and Eastern (EES) Ethiopian shields (Asrat et al. 2001; Stern et al., 2012; Verner et al., 2021). The WES is situated at the key location of the transition between the Arabian Nubian Shield to the north and the Mozambique Belt to the south (Abdelsalam and Stern, 1996) although there has been no consensus on the extent of the MB further north of Kenya (Fritz et al. 2013).

The MB mostly involved the re-cycling of older crustal material (gneisses and migmatites) and dominantly post collisional magmatism (Asrat et al. 2001; Fritz et al. 2013). The concentrations of granulitic rocks in the MB supports the interpretation that crustal thickening, erosion and intensity of deformation increased to the south. On the other hand, occurrences of granulite as far north as central Sudan suggests at least two episodes of granulite-facies metamorphism, Archean and Neoproterozoic (Stern and Dawoud 1991). According to Asrat et al. 2003, both the ANS and the MB shows late- to post tectonic granitic magmatism. The mafic-ultramafic, metavolcanics and metasedimentary rocks of Ethiopia are considered largely to be of oceanic provenance (Kazmin and Sukhorukov, 1988; Berhe, 1990), and spatially related to the Arabian-Nubian shield (Kazmin et al., 1978).

Arabian Nubian Shield (ANS)

The Arabian-Nubian Shield (ANS) constitutes the northern segment of the EAO exposing a large tract of mostly juvenile Neoproterozoic crust that were generated during the Pan-African orogenic cycle (Kroner et al., 2004). It formed as a result of a multistage process, whereby juvenile crust was produced above intra-oceanic convergent plate boundaries (juvenile

arcs) and perhaps oceanic plateaux (CU. 870-630 Ma). These juvenile terranes collided and coalesced to form larger composite terranes.

The ANS is composed of low-grade volcano-sedimentary rocks in association with plutons and ophiolitic remnants (Abdelsalam and Stern, 1996; Allen and Tadesse, 2003; Cox et al., 2012; Kröner et al., 1991; Robinson et al., 2014; Shackleton, 1996; Stern, 1994). The multiple geodynamic episodes in the ANS during the EAO were outlined by (Fritz et al., 2013): (a) sea-floor spreading (up to 830 Ma) followed by subduction and volcanic arcs and back arcs formation (ca. 890 to 750 Ma); (b) widespread crustal accretion followed by continent-continent collision (ca. 750 to 620 Ma) associated with polyphase deformation and a high- to low-grade metamorphic overprint and (c) late-orogenic extension corresponding to post collisional granite magmatism continuing up to ca. 550 Ma. In the ANS, a significant amount of older continental crust (Mesoproterozoic age crust) is also found such as the Afif terrane in Arabia and the Palaeo-Proterozoic and Archaean crust in Yemen that was overprinted by Pan-African tectono-magmatic events (Kroner et al., 2004). Several suture zones define the multi-stage assembly of the ANS among which the Northern (NES), Western (WES), Southern (SES) and Eastern (EES) Ethiopian shields fall in the southern ANS (Asrat et al. 2001; Stern et al., 2012; Fritz et al. 2013; Verner et al. 2021).

The southern ANS extends from southern Kenya to the Nakasib-Bir Umq suture formed first (Johnson et al., 2003). This part of the ANS constitutes terranes that are internally partitioned by arc-arc sutures (Kröner et al., 1991; Abdelsalam and Stern, 1996; Stern et al., 2010b and Johnson et al., 2011). Protolith ages from these terranes extend back to 900–830 Ma. The tectonic evolution of the southern ANS through a Wilson Cycle is well illustrated in the Tulu Dimtu belt of central Ethiopia (Woldemichael et al., 2010). According to Woldemichael et al., 2010; Early rifting was initiated between 900 and 860 Ma and then the transition from rifting to ocean floor spreading occurred between 860 and 830 Ma followed by the subduction and formation of arc- and back-arc basins occurred between 830 and 750 Ma; and finally, basin closure by accretion of island arcs commenced between 750 and 650 Ma. U–Pb zircon geochronological studies suggested that the Precambrian of southern ANS in Ethiopia is dominated by granitoids and orthogneisses emplaced between 900 and 550 Ma (Yibas et al., 2000).

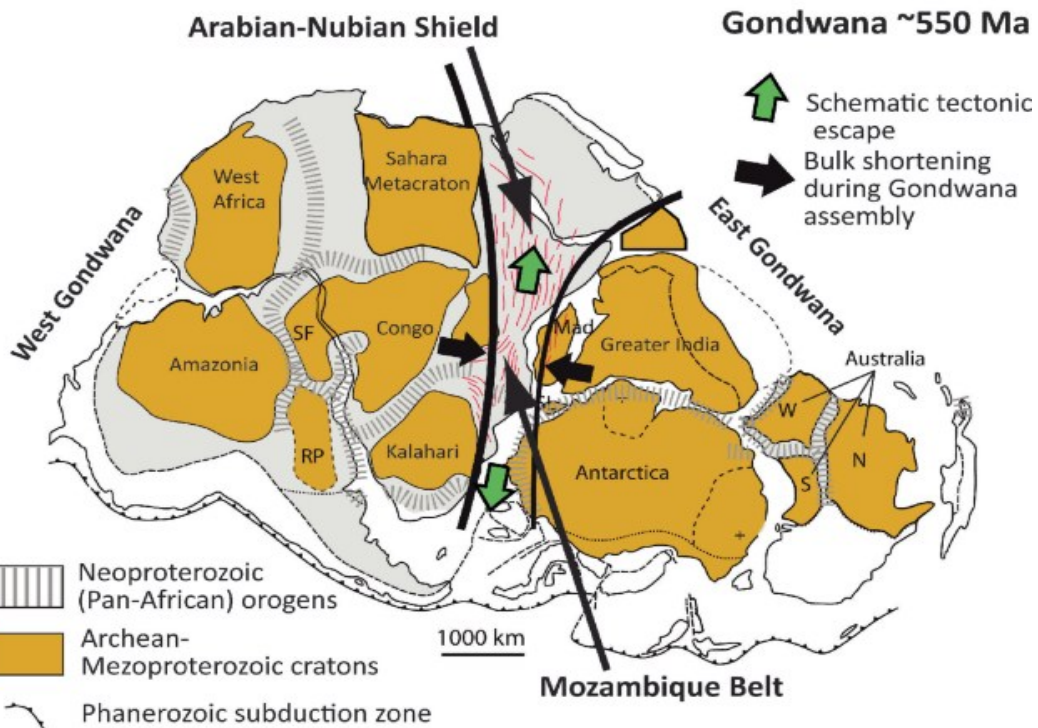
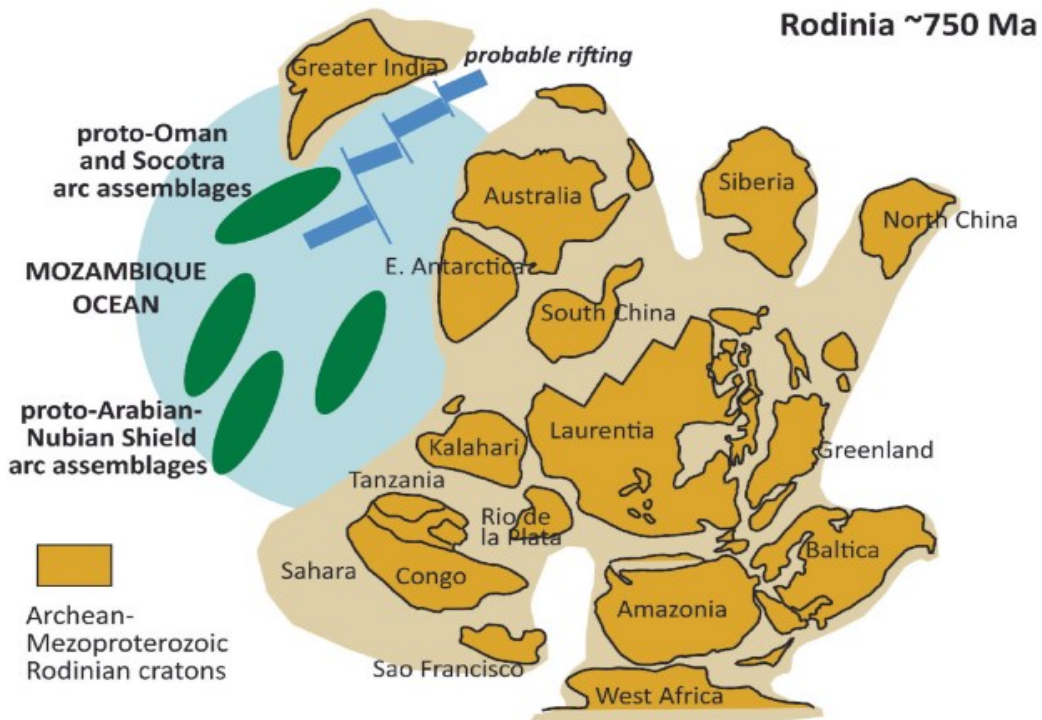


Figure 4. Historic Overview the Arabian-Nubian Shield (Peter R. Johnson, 2021).

Western Ethiopian Shield (WES)

Western Ethiopian Shield (WES) is situated as a key location close to the transition between the Arabian Nubian Shield and Mozambique Belt, adjacent, and east of the ‘Eastern Saharan Meta-craton’ (Abdelsalam and Stern, 1996). It was named as Tulu Dimtu Orogenic Belt which is composed of five litho-tectonic domains formed during the amalgamation of western Gondwana before the final closure of the Mozambique Ocean (Allen and Tadesse; 2003). These domains are Didesa, Kemashi, Dengi, Sirkole and Daka Domains. Didesa Domain is composed of moderate-grade polydeformed and metamorphosed gneisses intruded by deformed gabbroic and granitoid bodies and post-kinematic mafic and felsic plutons. Kemashi Domain has low-grade metasedimentary and ultramafic to mafic meta-volcanic rocks intruded by deformed and undeformed ultramafic-mafic and intermediate plutons. While Dengi Domain contains low-grade metasedimentary rocks, mafic to felsic metavolcanic rocks and moderate grade gneisses intruded by deformed and undeformed gabbroic to granitoid bodies. Sirkole Domain constitute alternating sequences of moderate grade polydeformed and metamorphosed gneisses and low-to moderate-grade metasedimentary rocks and mafic to felsic metavolcanic rocks. These rocks are intruded by deformed and undeformed granitoid plutons. Daka Domain are moderate-high grade polydeformed gneisses, intruded by syn-kinematic granitoids.

The intrusion of syn- and post- tectonic plutons into the Western Ethiopian Shield also useful to understand the tectonic evolution of the East African Orogen in Ethiopia. For example, Dabana granite pluton crystallization ages were determined through U–Pb geochronological dating and shows three intrusive periods under distinct tectonic domains that represent an evolving convergent margin (Bowden et al., 2020). The oldest granite dates to 797.6 Ma and associated with hydrous melting during volcanic arc subduction, followed by post-subduction related anhydrous magmatism at 774.6 Ma. The youngest granites date to 635–639 Ma and are evidence of late-stage crustal thickening in the final stage of collision.

Several geodynamic episodes in WES that were defined in the context of the ANS evolution are: (a) Early rifting of the Rodinia supercontinent associated with plume-type magmatism (ca. 900–860 Ma) continued by continental passive margin formation in the range between ca. 860 and 830 Ma (Woldemichael et al., 2010); (b) Subduction and volcanic arc formation ca. 830–750 Ma (Ayalew and Johnson, 2002; Woldemichael et al., 2010) gently overlapped with (c) high-grade metamorphism and migmatization in the collisional stage (dated

at ~775 Ma; Bowden et al., 2020) and anhydrous magmatism (dated at 774.6 Ma; Bowden et al., 2020). These events followed by (d) terrain accretion and syn-tectonic intrusions in the range of ca. 750–650 Ma (Woldemichael et al., 2010). The late-stage crustal thickening was constrained between ca. 650 and 635 Ma followed by later gravitational collapse associated with shearing and post-tectonic intrusions up to 550 Ma (Tsige and Abdelsalam, 2005; Ayalew and Johnson, 2002; Woldemichael et al., 2010; Bowden et al., 2020).

Southern Ethiopian Shield (SES)

Southern Ethiopian Shield (SES) is situated at the junction of the ANS and MB and has affinities to both. The nature of the transition between the MB and ANS which encompasses the region occupied by Ethiopia and Kenya is poorly defined (Hofmann et al., 1997). This is because the basement rocks of Kenya have not been studied with modern isotopic and geochronologic methods and Ethiopian basement rocks are mostly buried beneath Phanerozoic sediments and flood basalts of the Ethiopian Plateau erupted from the Afar mantle plume ~30 Ma ago. However, there is a ~200 km × 300 km region in southern Ethiopia where EAO basement is exposed that is why named as Southern Ethiopian Shield (SES). In southern Ethiopia, this event must have occurred between about 1050 and 880 Ma, as indicated by the oldest recognized metamorphic ages (Rb/Sr; Chater, 1971) and the earliest arc magmatism (Bulbul diorite; Yibas, 2000).

The geochronological data obtained from SHRIMP and Ar/Ar dating helped considerably to decipher the sequence of major magmatic and tectonothermal events that affected the Precambrian of southern Ethiopia between 900 and 500 Ma. According to Teklay et al., 1998; Worku et al., 1996 and Yibas et al., 2000; increasing geochronological database suggests that the Precambrian terrane is dominated by granitoids and ophiolites emplaced between 900 and 700 Ma, was followed by collisional granitic magmatism and coalescence between 700 and 550 Ma. The presence of Palaeoproterozoic “Pre-Mozambique Belt” crust in southern Ethiopia can, however, be inferred from xenocryst ages ranging from 2050 ± 82 to 1362 ± 43 Ma (SHRIMP, zircon ages, Yibas, 2000; for metarhyolite: 1125 ± 2.5 and 1656.8 ± 1.9 Ma using single zircon evaporation technique, Teklay et al., 1998). The U–Pb SHRIMP age of 526 ± 5 Ma obtained for the Metoarbesebat granite is interpreted as the magmatic emplacement age for the pluton, which is one of the youngest for the granitoids of southern Ethiopia.

Among several generations of granites in Ethiopia of Neoproterozoic, post-tectonic Konso pluton characterize the post-Pan-African evolution of the Mozambique Belt (MB) of southern Ethiopia. Age of pluton emplacement is constrained by a Rb–Sr isochron and zircon U–Pb data at 449 ± 2 Ma. Therefore, Konso pluton is the witness of an Ordovician A-type magmatic event, which marks a change from convergence related to the Pan-African collision, to extension in the Mozambique Belt of southern Ethiopia which was regarded as a Pan-African post-tectonic body (Davidson 1983). According to Davidson, 1983 and Verner et al., 2021; the plutons in hammar domain of southern Ethiopian shield were syn- to post tectonic intrusions. Therefore they suggest that Southern Ethiopian Shield has a juvenile origin far away from Cratonic sources derived from a volcano-sedimentary intra-oceanic magmatic arc of early EAO (ca. 770 Ma).

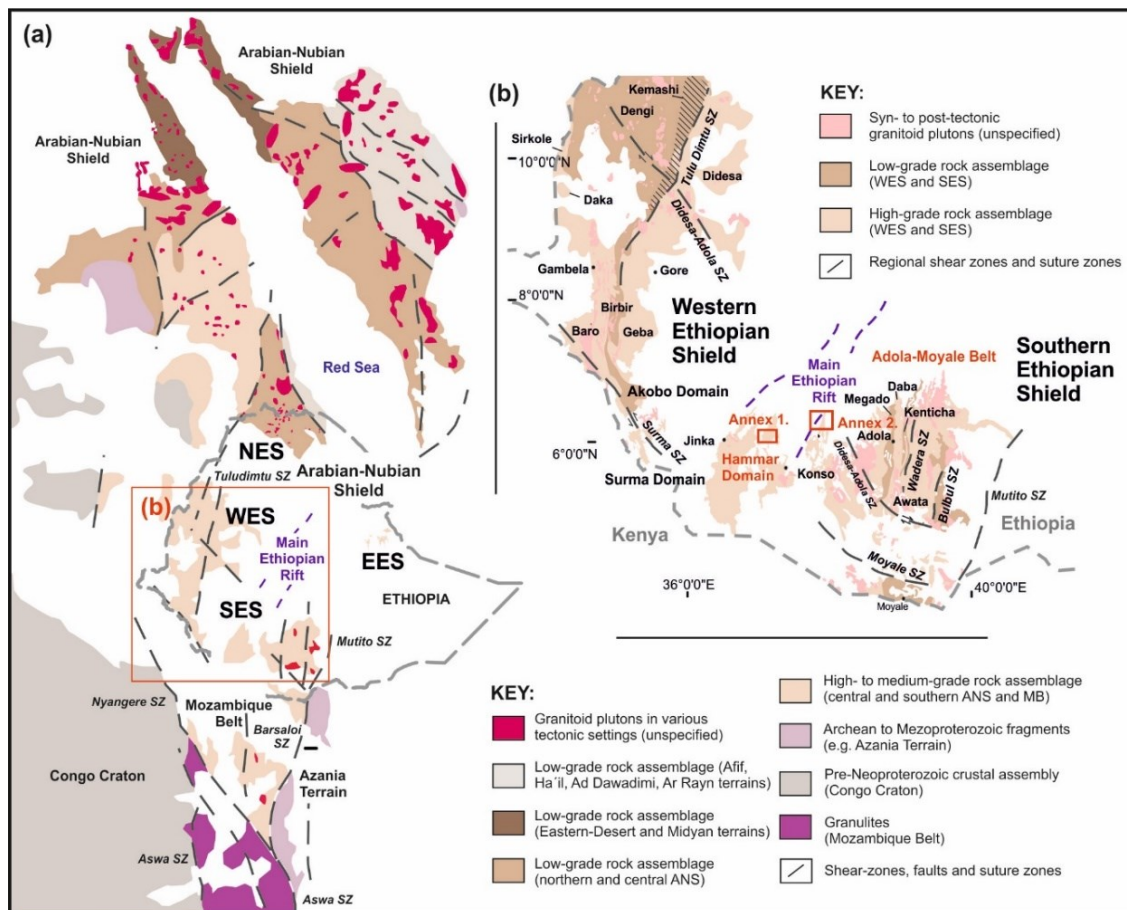


Figure 5. Sketch of Gondwana supercontinent assembly and position of ANS (modified after Fritz et al., 2013; Johnson, 2014); (b) Simplified geological map of the WES and SES including the Hammar Domain (modified after Davidson, 1983; Allen and Tade Tadesse, 2003; and Stern et al., 2012) and SES segments (Hammar Domain and Adola-Moyale Belts). Modified after Verner et al. (2021).

2.2. The study areas in the Southern Ethiopian Shield (SES)

Rocks of Southern Ethiopian Shield (SES) provides an opportunity to better understand the nature of the transition between ANS and MB and thus the evolution of the EAO in space and time. SES consists of two segments: (a) Adola-Moyale Belt and (b) Hammar-Surma-Akobo domains.

Adola-Moyale Belt

Adola-Moyale Belt is granite-gneiss basement interleaved with three belts (Megado, Kenticha and Bulbul) of low-grade greenschist-facies ophiolitic volcano-sedimentary rocks (Yibas et al., 2002). The Megado belt consists of metabasic and metasedimentary rocks which are dominantly ultramafic rocks. In southwestern Ethiopia of Adola belt zone Sebbeto tonalite and the Hiddi Asasu amphibolite indicate that they are products of late-Proterozoic magmatism in an island arc (oceanic) setting (Gichile et.al; 1993). Sebbeto tonalite appears to have differentiated from a primitive (mantle derived) melt. However, the Altuntu granite is emplaced at a continental plate margin that was in part thickened by magmatic underplating. This granite is derived from the partial melting of older magmatic rocks that underplated the continental margin during the early stages of the subduction process.

The Kenticha belt is composed of greenschist to lower amphibolite facies, semi-pelitic and graphitic schists, carbonaceous phyllite, marble, and mafic-ultramafic rocks. These rocks are locally intruded by late to post-tectonic two-mica granitic plutons (Yihunie and Tesfaye, 1998). The Kenticha and Megado mafic-ultramafic-sedimentary assemblages form two N–S trending linear Belts while the Bulbul Belt might represent a part of a regional, U shaped, folded ophiolitic belt (Kazmin, 1975) because the northern extension of the shear zone is intruded by a granitic body whereas its southern part terminates against a bow-shaped dextral strike slip shear zone.

The Bulbul Shear Zone is N–S trending belt and SW-verging fold-and-thrust belt at northern part with a dextral strike-slip shearing in the central part and normal faulting in the southern part (Abdelsalam et al., 2008). The Bulbul belt contains amphibole schist, metabasalt, ultramafic and semi-pelitic schists, which were metamorphosed under greenschist facies conditions (Tsige and Abdelsalam, 2005). The existence of the amphibolite schist, mafic and ultramafic, and meta-diorites in a distinct Chulul sub-domain has been interpreted as island

accretion evident from the arc-ophiolitic-plutonic association (Tsigé and Abdelsalam, 2005). The juxtaposed belts are all intruded by syn- to post-tectonic granitic, gabbroic and dioritic plutons, with N to NNW directed elongation and moderately E and ENE dipping foliation (Yihunie and Tesfaye, 2002).

The SES is dominated by four major tectonothermal events and contemporaneous magmatic episodes (Teklay et al., 1998; Yibas et al., 2002; Stern et al., 2012): (a) The late-Tonian to early-Cryogenian episode overlapping the Bulbul-Awata tectonothermal event (ca. 840–890 Ma) and (b) later the Megado tectonothermal event (ca. 770–700 Ma) both of which are associated with volcanic arc formation followed by (c) the Moyale tectonothermal event (ca. 660 Ma) and (d) the Ediacaran-Cambrian Pan-African episode (ca. 630–500 Ma) mainly related to the continental collision between East Gondwana and the consolidated Congo-Tanzanian-Saharan craton (West Gondwana). Crustal thickening driven by the continued ~E–W compression, triggered significant melting and the subsequent uplift over a wider region, involving shearing in the later stage as manifested by the Wadera shear zone dated at 580 Ma (Yibas et al., 2002).

According to Yibas et al. (2002), Yihunie and Tesfaye (2002), Allen and Tadesse (2003), and Yihunie and Hailu (2007), a W- and E-directed thrusting of individual units above the high-grade gneissic terranes are interpreted as an early phase of deformation between 800 and 650 Ma in Kenya and Ethiopia. This event was related to collision of the individual terranes after consumption of the Mozambique ocean along a possibly E-dipping subduction zone (the Bulbul and the northern Moyale belts; Tsigé and Abdelsalam, 2005). The N-trending strike-slip shearing was initiated soon after or contemporaneous with thrusting (Tolessa et al. 1991). The Adola-Moyale belt has been described as a positive flower structure (Tolessa et al. 1991; Ghebreab, 1992) and interpreted the southern ANS belts as a transcurrent orogen with an oblique NW–SE to NE–SW shortening components.

Late Precambrian rocks tectonic history and structural features of rock association of Moyale are part of the Mozambique Orogenic Belts (Tolessa et al., 1991 and Bonavia and Chorowic;1993; Ghebreab et al., 1992; Worku and Schandelmeier, 1996). Three deformation events are identified as: a) The re-folding of north-south trending early shears of upright, doubly plunging, tight to isoclinal folds (D_1 ; Barsaloian event of 580 Ma). It is subduction-related folding and thrusting, which culminated in the obduction of mafic-ultramafic assemblages onto

the passive continental margin sediments b) The collision of crustal blocks (D₂) leading to re-folding of D₁ structures and development of upright north- and northwest-striking faults probably reactivated as dextral shears during the northward expulsion of the Arabian-Nubian Shield from the Mozambique Belt (Burke and Sengor, 1986) and c) The initiation of the sinistral strike-slip shear zones (D₃) with N and NW strikes interpreted to be antithetic riedel shears (Worku and Schandelmeier, 1996) and N–S/ENE–WSW striking sinistral transcurrent shear zones and associated vertical folds (Ghebreab et al. 1992).

Surma-Akobo Domain

The Precambrian basement rocks in southwestern Ethiopia are composed of three major domains named as Akobo, Surma and Hammar which differ based on their deformation style, degree of metamorphism and lithological assemblages (Davidson, 1983). Akobo domain is formed by extensive granitoids of variable composition intruding into N–S striking medium-grade metamorphic schists and gneisses associated with mafic-ultramafic bodies (Davidson, 1983; Ayalew and Peccerillo 1998). Surma domain is characterized by penetrative NW–SE trending sinistral mylonite zone developed in biotite-hornblende gneiss, quartz-feldspathic gneisses, amphibolite and granulite (Davidson, 1983; Bonavia and Chorowicz, 1992).

Hammar Domain

Hammar Domain corresponds to the eastern sector of the south-western metamorphic terrain of Ethiopia that contains two major rock groups (Davidson, 1983): an older gneissic complex and several generations of plutonic suites of which the Konso pluton is one.

The gneissic complex comprises mafic, intermediate, felsic as well as metasedimentary gneisses and granulites, which were metamorphosed to middle-upper amphibolite and locally to granulite facies conditions with NE dipping superimposed regional metamorphic foliation (Davidson, 1983; Asrat and Barbey 2003; Verner et al., 2021). Gneisses are intruded by gabbroic, dioritic, and syn-, late- and post-tectonic granitic plutons (Davidson, 1983; Asrat and Barbey, 2003; Verner et al., 2021).

The rock assemblage of the area corresponds to the Hammar Domain forming ~NNW–SSE striking belts of gneissic complexes and several generations of plutonic suites (Asrat and Barbey 2003; Verner et al. 2021). The protolith of metamorphic rocks are older granitic crust

that occupied southwestern Ethiopia prior to ca. 1000 Ma. The plutonic rocks occur as discrete bodies of gabbros, diorites, syn-, late- and post-tectonic granites accompanied by leucogranite, aplite, and pegmatite dikes (Asrat and Barbey 2003). The gneissic rocks are strongly and steeply folded, and show regional NNW–SSE trending foliations with steep NE dips. According to Davidson, 1983 and Bonavia and Chorowicz ,1992; the Hammar Domain forms an anticlinorium with an axial plane dipping steeply to the east. Based on different lithological types, mineralogical and textural characteristics as Hammar Domain can be divided as high grade rocks and Granite plutons and other intrusives (Davidson, 1983).

Granite plutons and other intrusives includes plutonic rocks occur as discrete bodies of ultramafic rocks, gabbros, diorites, syn-, late- tectonic granites accompanied with leucogranite, aplite and pegmatite dikes. The high-grade metamorphic complex is intruded by *syn*-tectonic foliated biotite granites. The medium- to coarse-grained often porphyroclastic metagranites consist of anhedral quartz, subhedral plagioclase, anhedral to subhedral long K-feldspar and biotite, with subordinate quantities of zircon, apatite, monazite and ilmenite. Medium-grained, foliated biotite syenite is composed of perthitic alkali feldspar, plagioclase, and quartz, with minor biotite. The medium-grained, muscovite-biotite and muscovite-garnet leucogranites consist of anhedral quartz, K-feldspar, plagioclase, biotite, muscovite and/or garnet. Their accessory minerals include zircon, apatite, monazite and ilmenite.

Hammar Domain reflects similar geodynamic episodes as the Adola-Moyale Belt involving early rifting and passive margin development (ca. 1100–1000 Ma; de Wit and Chewaka, 1981; Davidson, 1983; Gichile, 1992), west-dipping subduction associated with volcanic arc formation at ca. 900–750 Ma, followed by crustal extension (ca. 750–650 Ma) and a collisional stage and uplift between 650 and 450 Ma. The post-collisional magmatism was inferred from the emplacement of the A-type Konso pluton dated at 449 ± 2 Ma; Asrat and Barbey, 2003). The tectono-metamorphic evolution of the Hammar Domain has been summarized by Verner et al. 2021 into four phases as: a) formation of volcanic arc dated at ca. 770 Ma of late Tonian to late Cryogenian. b) formation of crustal accretion related with intense migmatization and HT-MP metamorphism (T: 700–850 °C and P: 0.7–0.9 GPa) at depths of ~25–35 km dated at ca. 720 and 715 Ma. The zircon data of granulites (721 ± 12 Ma; SHRIMP U–Pb method and 728.6 ± 0.6 Ma; Pb–Pb evaporation method) determined by Teklay et al., 1998 were interpreted as the age of the protolith. c) late Cryogenian to early Ediacaran episode dated from ca. 650 to 620 Ma of continental collision is related with formation *syn*-tectonic

granitoid intrusions yielded at ca. 648 Ma and ca. 630 Ma respectively. d) syn- to post-tectonic leucogranite dyke dated at ca. 630 Ma marks the upper limit for the ductile or brittle-ductile deformation and regional metamorphic events. The structural evolution of the Hammar Domain can be summarized into four phases of deformational events as D₁ to D₄ (Verner et al., 2021) resulted in (a) relict compositional banding (S₁), (b) flat-lying migmatite foliation (S₂) defining the primary contacts of granulites and migmatites, (c) superimposed steeply dipping N–S trending compressional foliation (S₃) due to regional ~E–W oriented compression and (d) later ~NW–SE trending left-lateral transpressive fabric (S₄).

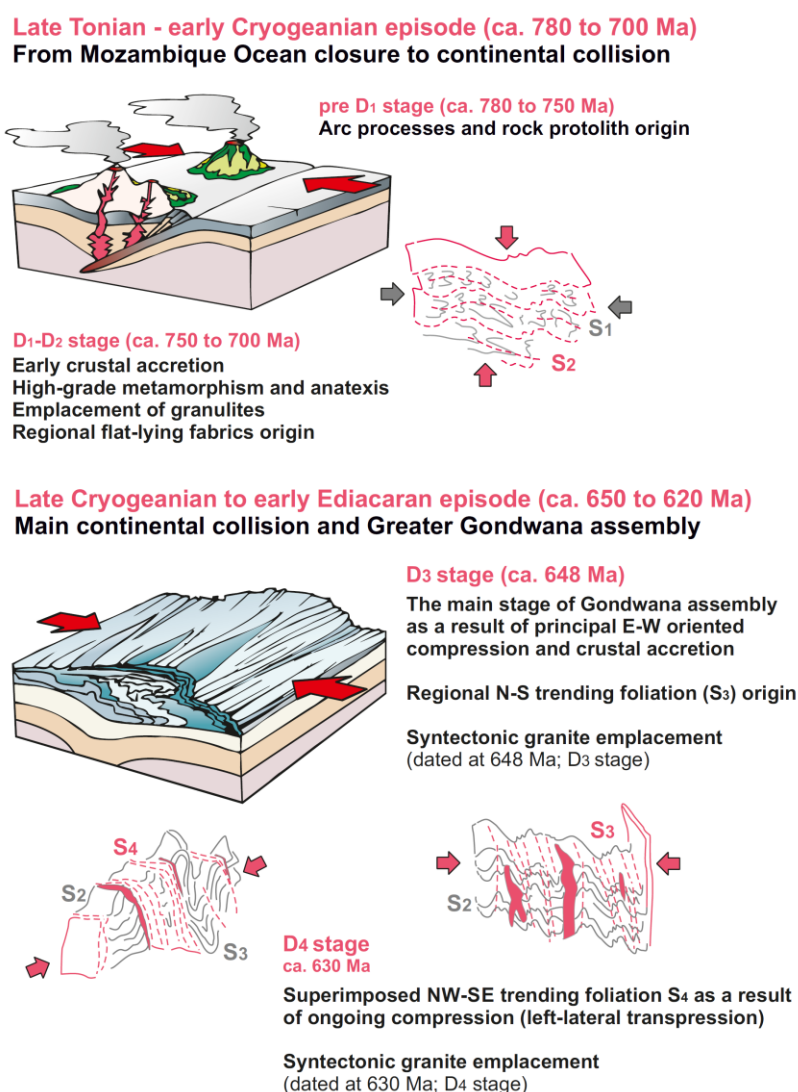


Figure 6. Scenario of geodynamic evolution of the Hammar Domain (Southern Ethiopian Shield) in the context of East-African Orogeny (according to Verner et al. 2021).

3. Methodology

3.1. Field work and data collection

The field geological mapping of the study area (southeastern part of the Sidama Region and southern Gamo Zone) was done on a scale of 1:100,000 by the Czech Geological Survey (CGS) and Geological Survey of Ethiopia (GSE) in frame of the development aid project “Ensuring Sustainable Land Management in Selected Areas of Ethiopia on the Basis of Geoscientific Mapping”, funded by Czech Development Agency. The major objective was to comprehensively characterize the natural environment with respect to the efficient and safe utilization of natural resources including soil, groundwater, and mineral resources, and also interaction with the geo-hazards.

The field work and the subsequent compilation of the geological map (Annex 1, 2) as well the structural analysis took place in cooperation with the solution of the Czech Development Cooperation project in the years 2020 to 2022. The partial results obtained as part of this work are part of the compilation work from the Sidama region (Verner et al. 2022) and Gamo zones (Verner et al. in preparation). The detailed methodology of field geological research and the compilation of a geological map is based on the work of Hanžl and Verner eds. (2018).

3.2. Remote sensing analysis and morphotectonic

Digital Elevation Model (DEM) was derived from ASTER imagery, Shuttle Radar Topographic Mission (SRTM-3), and Landsat 7 Enhance Thematic Mapper (ETM+) for the morphotectonic analysis. SpheriStat 3 is used for doing structural pattern on the rose diagram to compare their orientations. ASTER DEM image was generated using [®]ArcMap 10.6 (www.esri.com). Remote sensing analysis of optical imagery of various spatial, spectral and temporal resolution are also useful for geoscientific mapping. These optical imageries are Sentinel-2 data with an exceptional spatial resolution of 10 meters for VIS-NIR bands, Landsat 8 with the longest continuous satellite sensing mission and ASTER with the best spectral resolution among freely available satellite data. Sentinel-2 imagery has a spatial resolution of 10 meters and uses *Principal Component Analysis (PCA) and vegetation masked out* while Landsat 8 imagery has a standard spatial resolution of 30 meters use band combination (*bands*

7, 6, 5 – SWIR–SWIR–NIR) for identification of lithological contacts in the Gamo Zone (Figure 7) and Sidama Region (Figure 8).

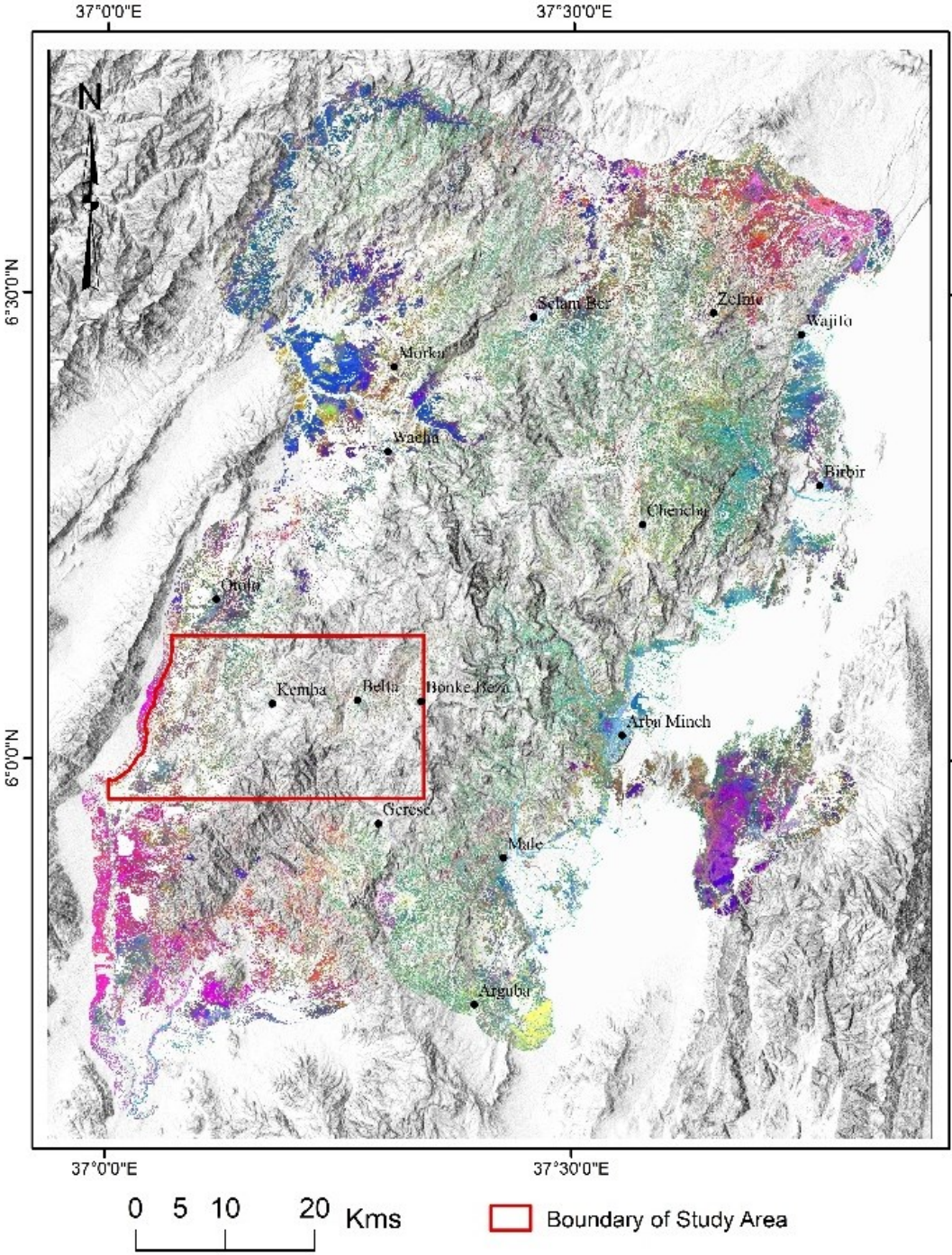


Figure 7. The example of Principal Component Analysis (PCA) transform of the Sentinel–2 imagery, vegetation masked out of the Gamo Zone. Color variation shows various types of soils, volcaniclastic deposits and lithological units.

Here Color variation shows various types of soils, volcanoclastic deposits and lithological units. Brownish and reddish color represent clay minerals and iron-oxides, green color represents iron-oxides while blue color represents iron-hydroxides.

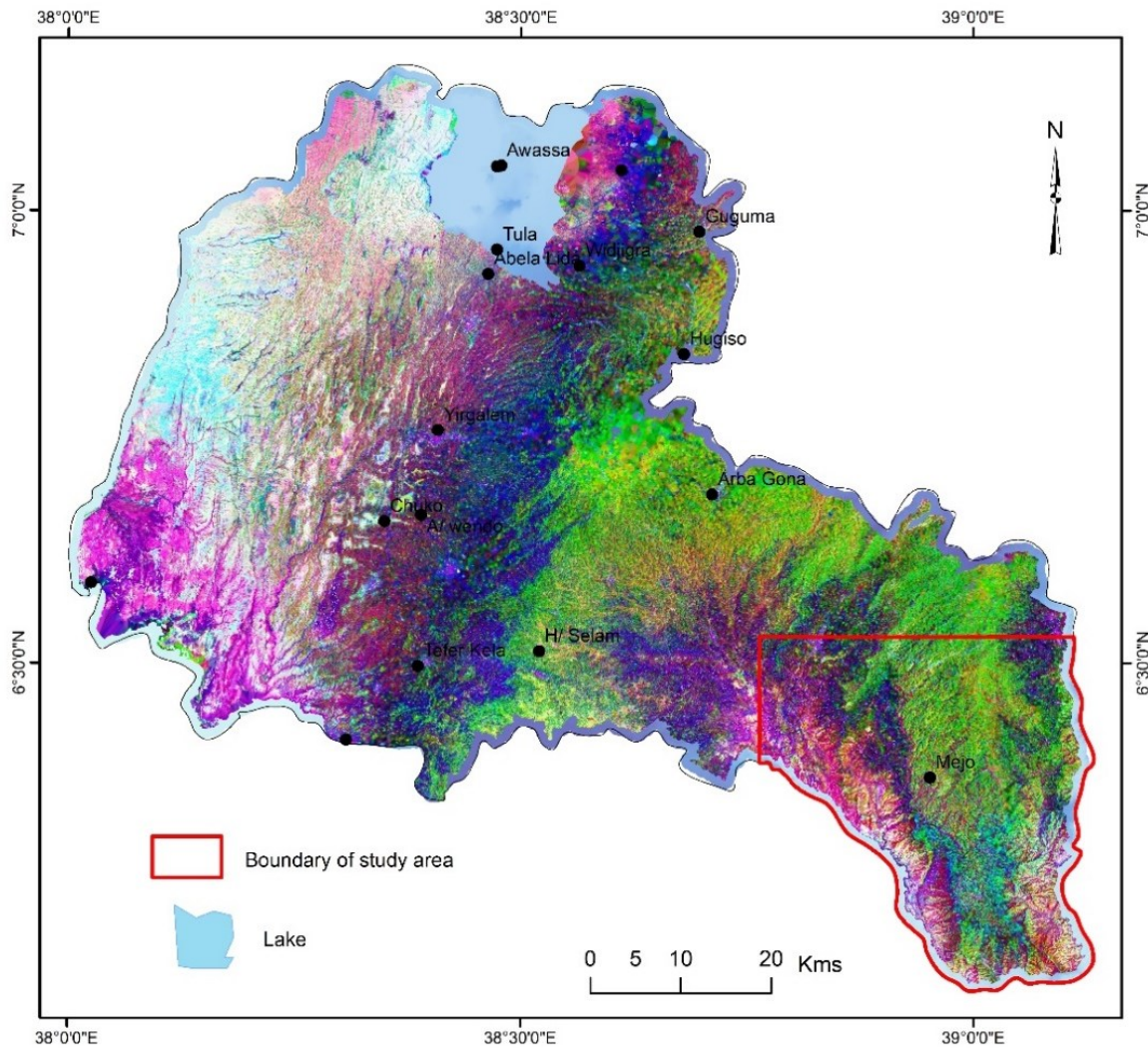


Figure 8. Principal Component Analysis (PCA) transform of the Sentinel-2 imagery, vegetation masked out of the Sidama Region. Color variation shows various types of soils, volcanoclastic deposits and different lithological units.

3.3. U-Pb dating

The rocks sample was crushed on a jaw crusher and homogenized. Zircon grains were separated by sieving. Next, zircons were selected according to morphological features and prepared for analytical work. The structure of selected zircons was visualised using cathodoluminescence (CL) at the Czech Geological Survey. Pb and U isotopic ratios were measured on a mass basis of an Inductively Coupled Plasma Spectrometer (ICP-MS). The Laser Ablation equipment comprises an Analyte Excite 193 nm excimer laser (Teledyne Cetac), which is connected to an Agilent 7900x Quad ICP-MS. The laser beam frequency was 5 Hz, beam diameter 30 μm , fluence 4–5 $\text{J}\cdot\text{cm}^{-2}$. Elemental fractionation and instrumental mass discrimination were corrected by normalization to the internal natural zircon U-Pb standard Plešovice (Sláma et al. 2008) and by the reference of natural zircon U-Pb standard GJ-1 (Jackson et al. 2004). Both standards provided data within the analytical framework errors consistent with U-Pb data.

4. Morphotectonic analysis

Morphotectonic analysis was done based on the digital elevation models (DEM) and ASTER and the Shuttle Radar Topographic Mission (SRTM-3) data by the combination of Landsat 7 ETM+ image. ASTER DEM image was generated using ArcMap 10.6 software (www.esri.com). The prominent morphological features have been identified using this method are the regional faults, fault zones and extensional joints. In some cases, the asymmetric ranges, slopes or/and scarps commonly correspond to the regional rift-related faults which are responsible for a displacement of Pleistocene and Neogene lithological boundaries. The images were compared with field geological mapping data to distinguish active fault scarps from differential erosion of contrasting lithologies.

The ‘linear indices’ image was generated which represents active faults with normal and normal-oblique slip, and in a few cases also probable strike-slip faults. However, there is lack of field verification in some cases and the “linear indices” may represent prominent fracture zones or lithological boundaries in some areas. Shaded relief maps, derived from DEMs with NW, N and NE direction of illumination, and multidirectional shaded relief maps were used as the base map for morphotectonic interpretation. Thus, interpreted lineaments are mostly represent as active faults, fault zones, fracture zones and also older faults with a prominent lithological contrast can be also reflected in the morphology.

The morphotectonic pattern of southwestern Gamo Zone is characterized by prominent ~NNE(NE)–SSW(SW) and ~NW–SE striking lineaments (Figure 9) mostly representing the major normal faults of the region. Based on frequency in orientation of lineaments (Figure 10a) the orientation of faults are aligned parallel to the main normal faults and escarpments of the Main Ethiopian Rift System trending ~NNE(NE)–SSW(SW). The second orientation maxima of morpho-lineaments found in ~WNW(NW)–ESE(SE) direction represents a subordinate set of oblique-slip or normal faults which are perpendicular to the rift system.

The southeastern part of the Sidama Region (Adola-Moyale Belt) is characterized by very deep valleys incised to the Precambrian basement overlaid by Eocene to Pleistocene volcanites and volcanoclastic deposits. The lineaments have been identified here reveal prevailing ~N–S and ~ENE–WSW trends (Figure 11). The frequency in orientation is also shown on rose diagram to indicate the alignment of linear indices (Figure 10b).

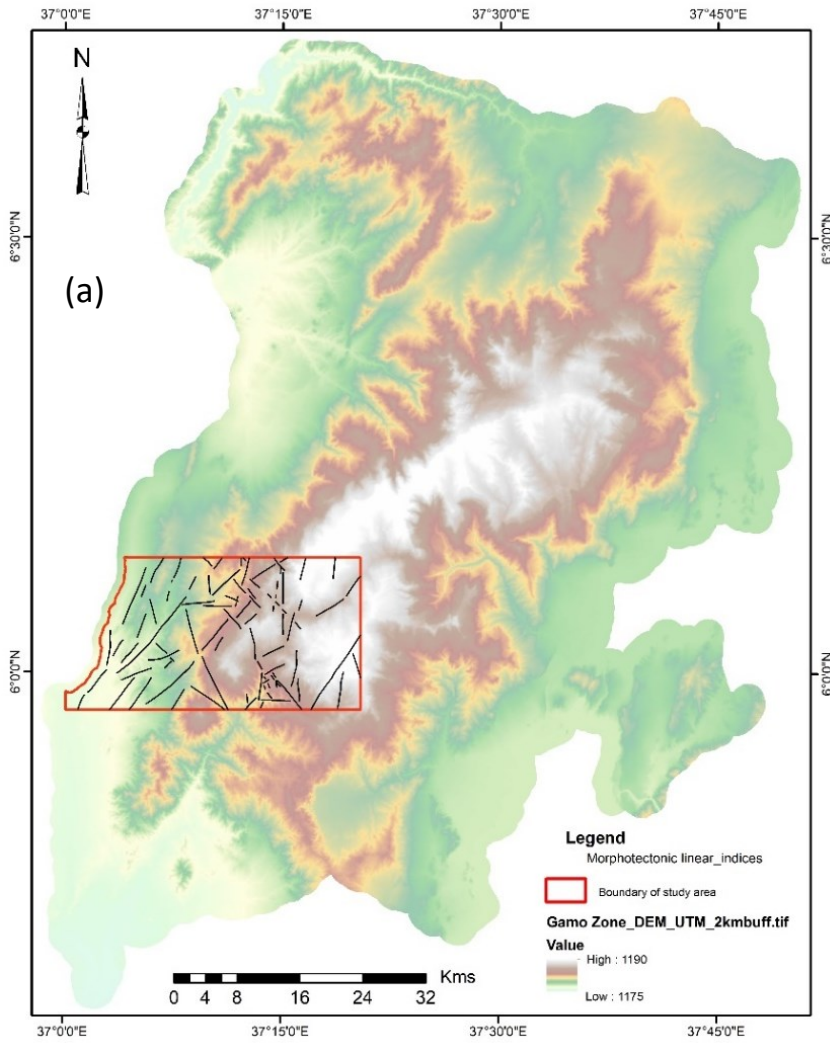


Figure 9. Digital elevation models (DEM) of the Gamo Zone with interpretation of morphotectonic linear indices on the study area (red polygon).

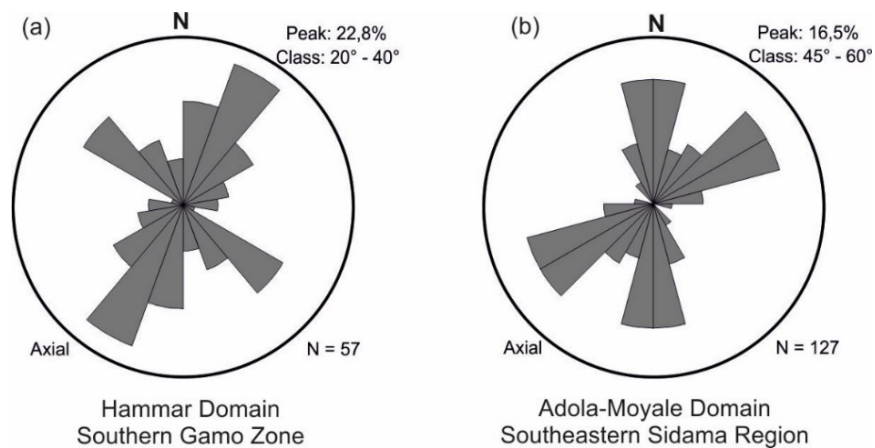


Figure 10. Rose diagram showing the orientation frequency of linear indices (morpholineaments): (a) Southern Gamo Zone and (b) Southeastern Adola-Moyale Belt.

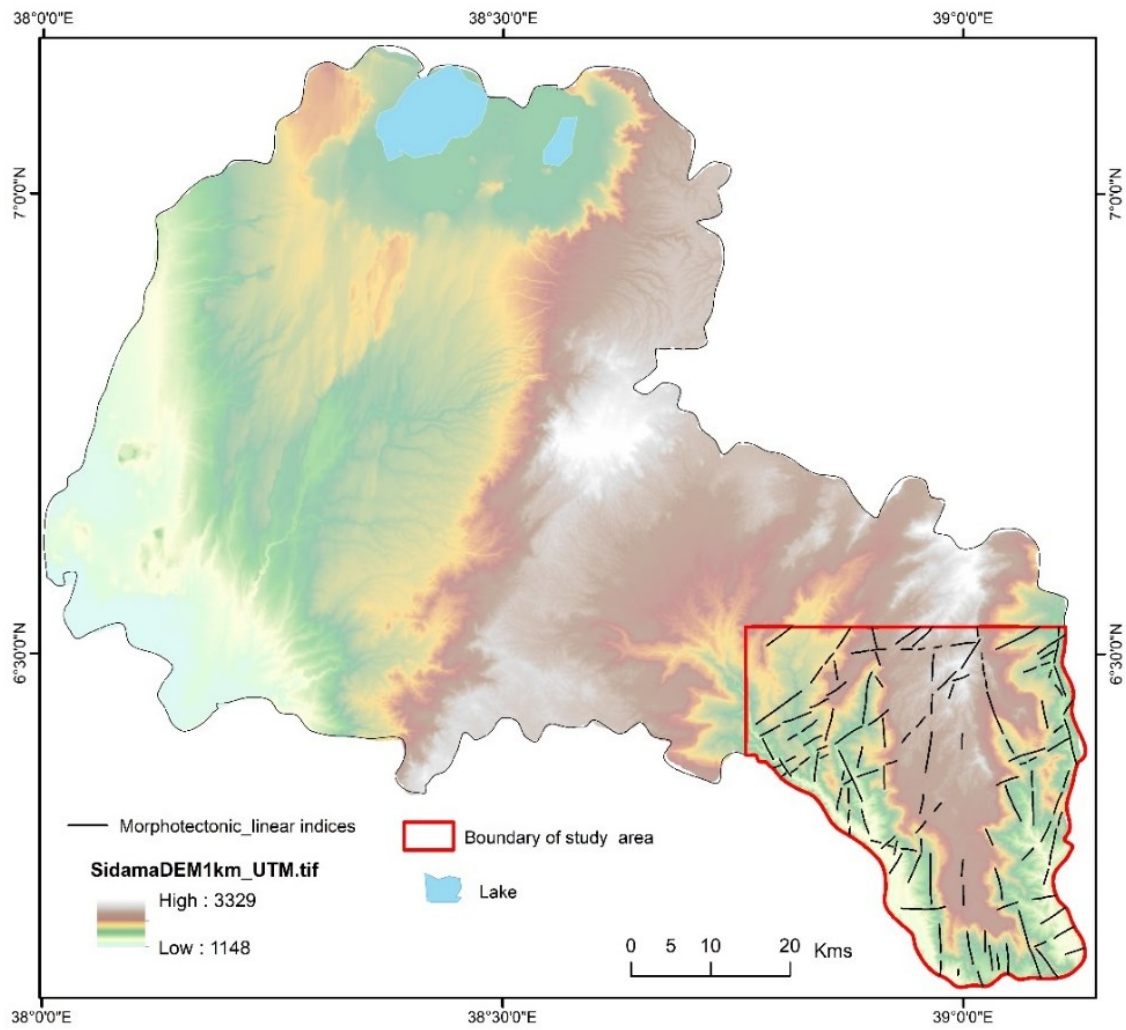


Figure 11. Digital elevation models (DEM) of the Sidama Region with interpretation of morphotectonic linear indices on the study area (red polygon).

5. Lithology

The studied area in southwestern part of the Gamo Zone and southern Sidama Region is built by different lithotectonic units (Figure 12). The oldest one includes the high- to medium-grade rock assemblage of Neoproterozoic age belonging to the Southern Ethiopian Shield (SES). The southwestern part of the Gamo Zone is composed of migmatites, amphibolites and paragneisses belonging to the northern Hammar Domain (Figure 12; label “a”). The southeastern Sidama Region is built by paragneisses, amphibolites, orthogneisses and schists forming the northwestern tip of the Adola-Moyale Belt (Figure 12; label “b”). These both units of Neoproterozoic rocks are overlaid by Cenozoic volcanic and volcanoclastic sequences of the Main Ethiopian Rift (MER). The overall lithological pattern is described successively as follows.

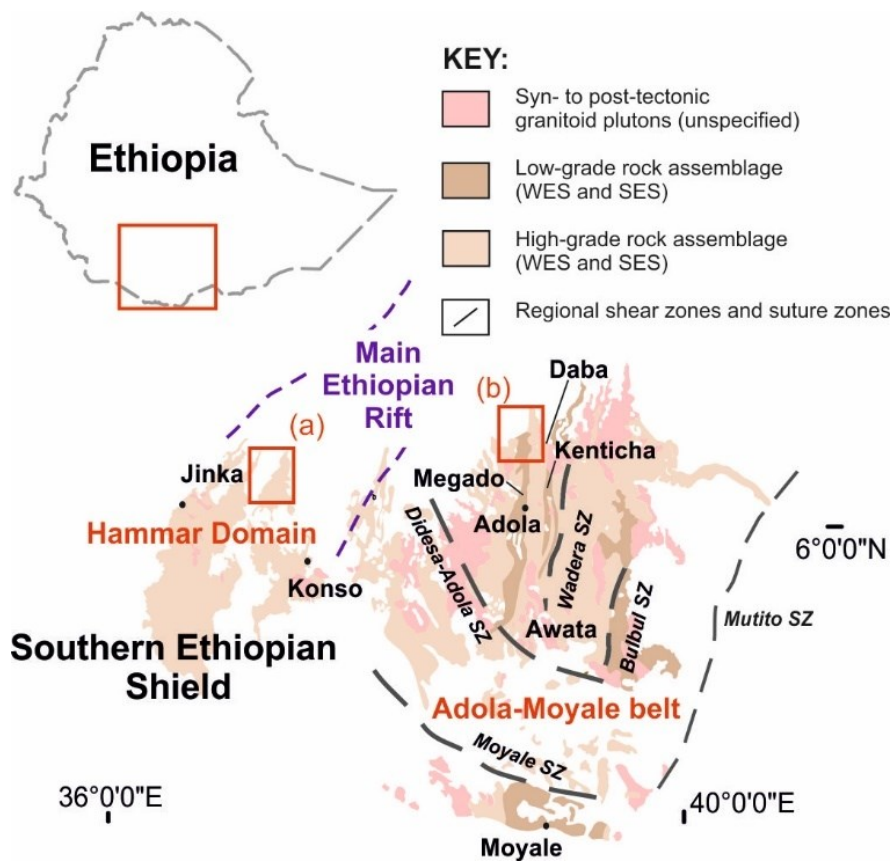


Figure 12. Schematic sketch of the Southern Ethiopian Shield (SES) and position of both studied areas (a) the southern Gamo Zone (Hammar Domain) and (b) southeastern Sidama Region (Adola-Moyale Belt).

5.1. Northern Hammar Domain of Gamo Zone (Neoproterozoic basement rocks)

In the first studied area (southern Gamo Zone; Figure 13) located westward of the ~NNE–SSW trending Main Ethiopian Rift (MER) several lithologies of high-grade rocks such as orthogneisses, amphibolites, migmatites and migmatized paragneisses and granite intrusives were mapped. According to the legend to geological map which is the result of this thesis (Annex 1) following lithologies are briefly described.

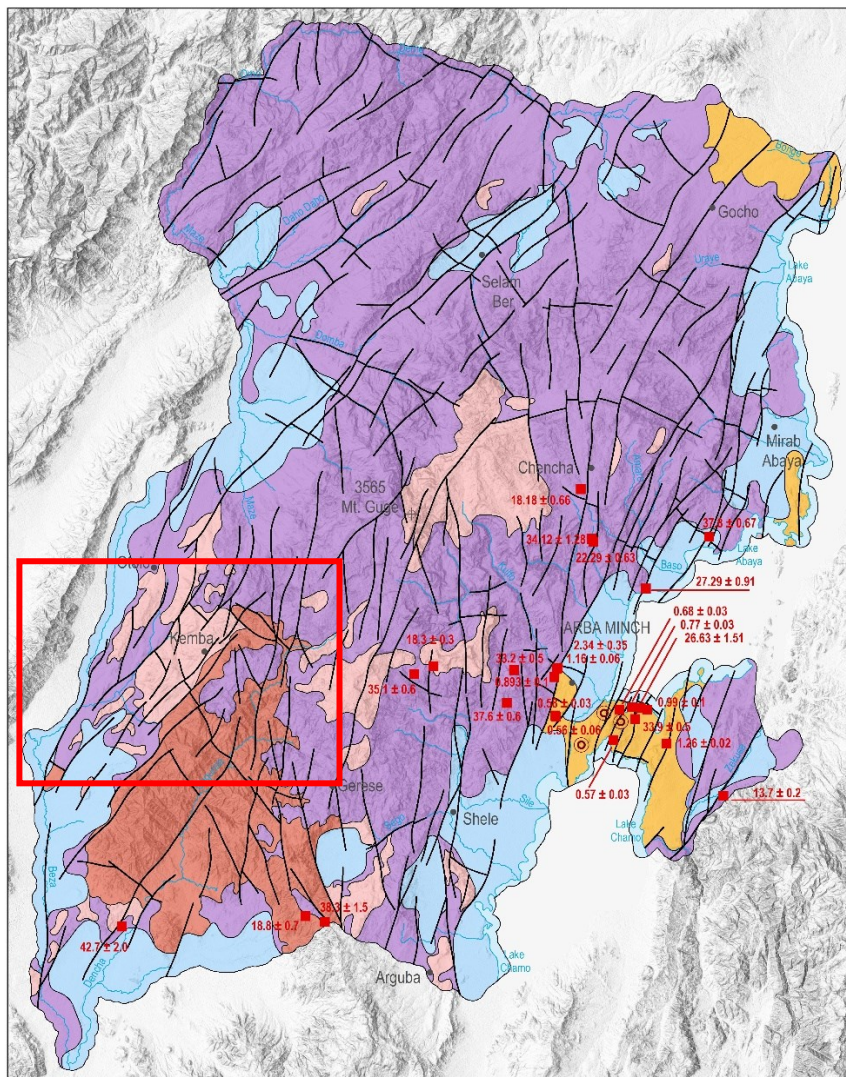
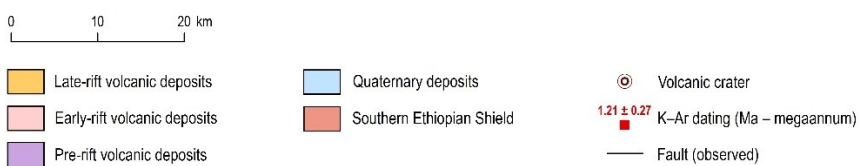


Figure 13. Simplified sketch the Gamo Zone including the main lithotectonic units and the extent of the studied area.



The ***biotite to amphibole-biotite orthogneiss*** is medium-grained, light-gray rock having equigranular or porphyroclastic, with a variable degree of ductile deformation (Figure 14). Orthogneiss is dominantly composed of quartz, plagioclase, K-feldspar and biotite. ***Amphibolite*** forms an elongated body within the metasedimentary sequence (gneiss with variable degree of migmatization) forming ~NNW–SSE trending belts. The rock is massive, intensely fractured, and dark grey in color. The dominant composition includes amphibole, plagioclase, minor quartz, biotite and epidote-clinozoisite. In addition, locally banded amphibolite is present, characterized by alternating several cm thick leucocratic and dark amphibole-rich layers (Figure 15). ***Migmatite and migmatized biotite paragneiss*** is exposed in the southern and central part of the area. It is a medium- to fine-grained, dark gray rock with a variable content of leucosome and non-foliated leucogranite veins/pockets up to 50 cm are locally observed. The ***biotite to muscovite-biotite paragneiss*** is medium-grained, dark-gray paragneiss displays a well-developed metamorphic foliation forming ~NNW–SSE trending belt in the southern part. The major minerals are plagioclase, quartz, biotite and often also muscovite. The ***biotite and amphibole-biotite granodiorite to tonalite*** forms a body at the contact of the gneisses and amphibolites at southern part of the area. The medium- to coarse-grained, often porphyroclastic granodiorite to tonalite. It consists of anhedral quartz, subhedral plagioclase, anhedral to subhedral 1–2 cm long K-feldspar, biotite and locally also amphibole. The ***muscovite-biotite granite*** occurs at the contact of gneisses and migmatites northern part of the area. It is fine- to medium-grained, equigranular, often leucocratic granite. It consists of quartz, K-feldspar, plagioclase, biotite and muscovite.



Figure 14. Field photograph of medium-grained biotite orthogneiss (south of Geresse).

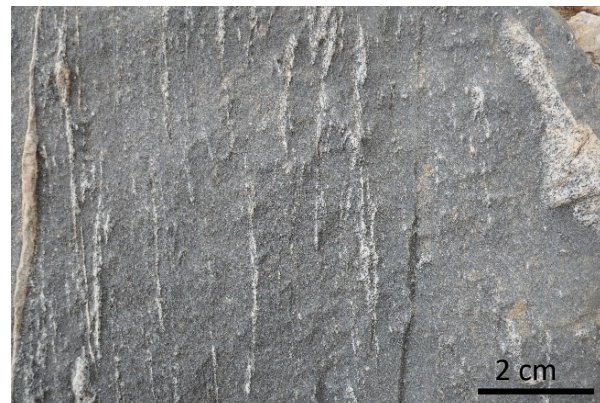


Figure 15. Field photograph of amphibolite with irregular bands of leucosome (south of Kemba).

5.2. Northwestern Adola-Moyale Belt of Sidama Region (Neoproterozoic rocks)

In the second studied area (southeastern Sidama Region; Figure 16) localized east of ~NNE–SSW trending Main Ethiopian Rift (MER) the high-grade lithologies such as orthogneisses, amphibolites, migmatites and migmatized paragneisses, paragneisses, schists and plutonic rocks were identified. According to the legend to geological map (Annex 2) below a brief description of main lithologies is listed.

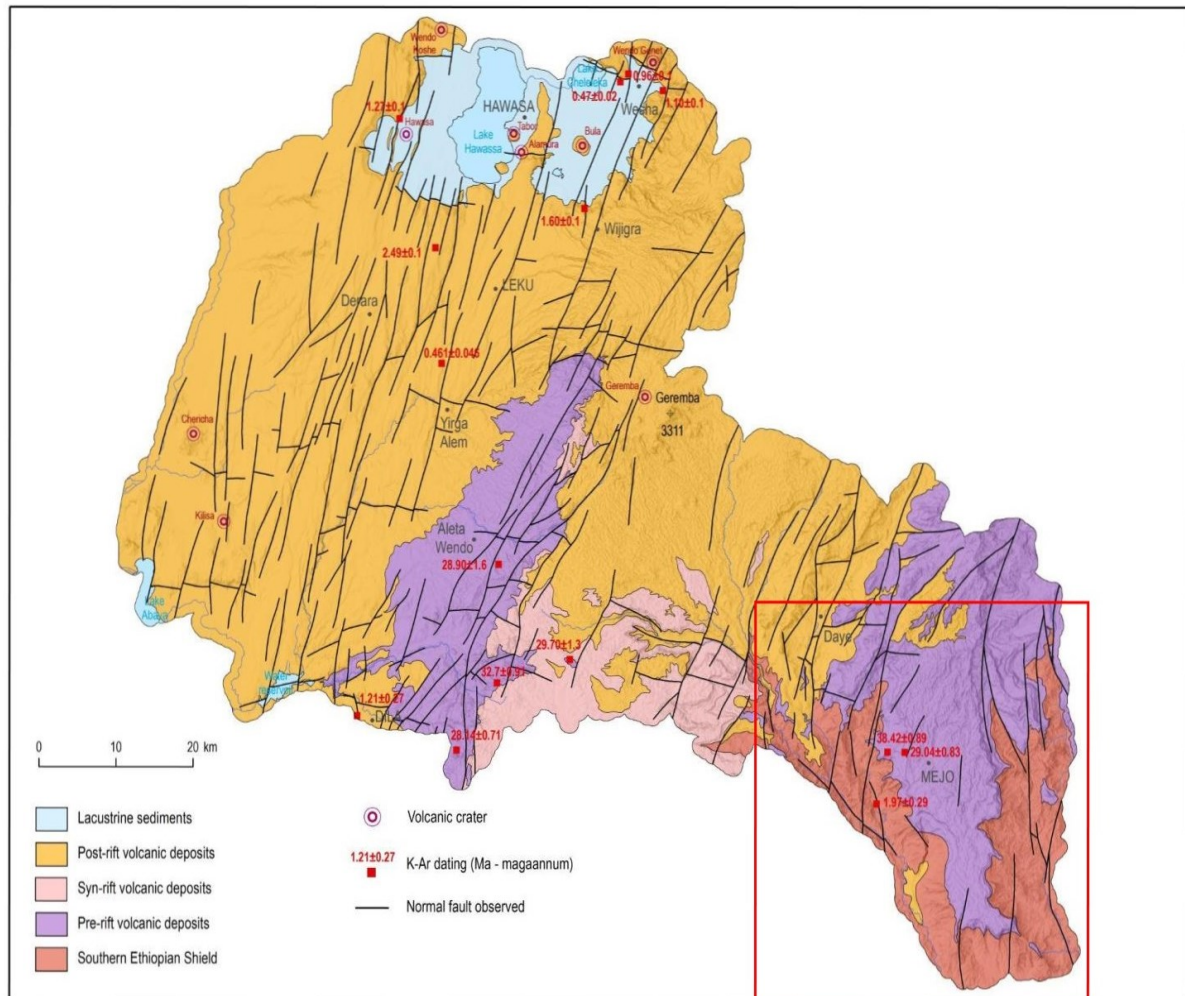


Figure 16. Regional simplified geological schematic map of the Sidama Region (Verner et al., 2022). Red rectangle shows the boundary of study area.

The **biotite to amphibole- biotite orthogneiss** is medium and rarely fine grained, light gray orthogneiss locally porphyroclastic. There is mafic microgranular, fine-grained, elongated enclaves up to 20 cm in length which have a higher content of biotite (and often also epidote) are locally present. Orthogneiss is dominantly composed of quartz, plagioclase, K-feldspar and biotite and locally of minerals of the epidote-clinozoisite group. In some strongly deformed

orthogneiss samples, several mm thick strips with biotite or quartz dominant assemblages are visible. *Migmatite and migmatized biotite paragneiss* are situated within the complex of paragneisses and orthogneisses in the southern part of the area. It contains foliated concordant leucosome rich stromatitic migmatites dominantly. It is composed of quartz, k-feldspar, plagioclase and biotite. Variation in grain size between layers is from fine- to medium- grained. *Sericite schist* is fine grained, pale-gray to yellowish, strongly foliated rock spatially related to quartz hydrothermal veins exposed at southwestern part. Sericite schist consists of muscovite, quartz, plagioclase, pyrite, magnetite, chlorite and kyanite. Quartz veins parallel with the foliation is also common in this rock. The *Biotite to muscovite- biotite paragneiss* is exposed in the valley of the Genale River in southeastern part of the area. It is a medium- to fine grained and dark gray rock (Figure 17). It is composed of biotite, plagioclase and quartz over the other rock-forming minerals such as muscovite, K-feldspar and subordinate tourmaline and/or garnet. *Biotite-muscovite phyllite locally with graphite* forms at the contact of paragneisses and amphibolite in the area. It has dark gray to pale- gray, fine grained, foliated rock consists of alternating layers of quartz and muscovite that are visible along the biotite (chlorite) aggregates. Graphite and iron oxides are also present within the complex of biotite paragneisses. It is a medium- to fine grained, dark grey, and strongly foliated rock. *Amphibolite* forms N–S trending belts in valleys of the Logita and Genale rivers at western part of the study area. The dominant type is banded amphibolite which is characterized by alternations of several cm thick leucocratic and amphibole- rich (melanocratic) layers (Figure 19). It consists of amphibole, plagioclase, epidote-clinozoisite, quartz, biotite, garnet biotite and opaque minerals (magnetite and/or ilmenite).



Figure 17. Field photograph of biotite to muscovite-biotite paragneiss (Genale River).

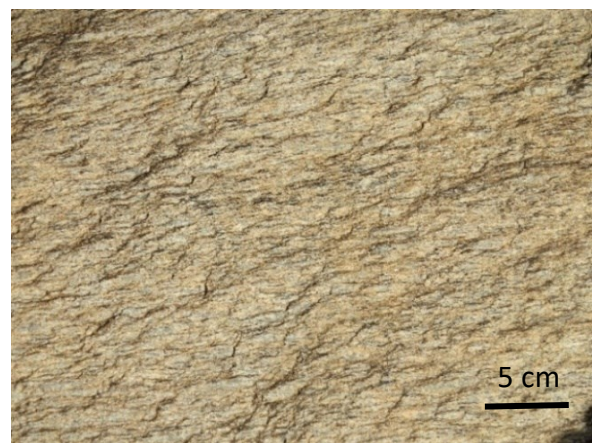


Figure 18. Field photograph of medium-grained foliated biotite orthogneiss (south of Girja).

The ***Talc-tremolite to chlorite schist*** exposed at western part of the area (e.g. around the peak of Bubisa) showing medium- to fine- grained, green to whitish- green, strongly foliated rocks that are composed mainly of talc and tremolite. Elongated crystals or radial aggregates of tremolite needles up to 5 cm long are sometimes visible in the hand specimen. ***Serpentinized peridotite and metagabbro*** form in talc-tremolite to chlorite schists of few to several hundred meters in size. Serpentinized peridotite to serpentinite is a fine-grained, greenish to rusty rock composed mainly of serpentine minerals and magnetite. Metagabbro shows a medium- to coarse-grained texture. It is composed of amphibole, plagioclase, pyroxene, epidote and magnetite. Sometimes, it also shows a cumulate texture of amphibole-rich layers and spots of several m in size. ***Muscovite-biotite granite*** forms a small body within biotite to amphibole-biotite orthogneiss in the southern part of the area and it is medium to fine-grained granite. It is composed mainly of quartz, K-feldspar, plagioclase, and micas. The ***Biotite granodiorite*** forms small N–S oriented intrusions in the southern part of the area. It is brown-gray to pink-gray equigranular to slightly porphyritic granodiorite. composed of percent plagioclase, K-feldspar, quartz and biotite. ***Quartz veins*** have been found in all the metamorphic lithologies (commonly up to 3 meters in thickness). Their contacts are sharp, mostly discordant to the regional fabrics. Quartz hydrothermal veins are composed of homogeneous milky to grayish white quartz.



Figure 19. Field photograph of banded amphibolite with isoclinal folds of leucosome (Genale River).

5.3. Cenozoic volcano-sedimentary sequences of the Main Ethiopian Rift

Cenozoic volcanic sequences exposed on the study areas (Annex 1 and Annex 2) is divided two major units:

(a) **Pre-rift effusive rocks** and volcanoclastic deposits of Eocene to Oligocene ages. This sequence consists of several compositionally different rocks such as e.g. the Amaro-Gamo basalts interleaved by ignimbrites and acid pyroclastic deposits.

(b) **Early-rift volcanic deposits** of Neogene age (Miocene to Pliocene) including alkali basalt to trachybasalt and trachyte lava flows and associated pyroclastic deposits interleaved by rhyolites.

Pre-Rift volcanic lava flows and volcanoclastic deposits (Eocene to Oligocene)

The lithologies are described successively according to stratigraphy, from the oldest to youngest. *The sandstones* form discontinuous, up to several meters thick strata located below pre-rift volcanic and volcanoclastic deposits. The dominantly red to reddish sandstones locally passes into clast-supported quartz conglomerate to breccia strata of up to 1 m thick, hematite ore strata of up to 0.3 m and contain angular volcanic clasts and/or layers of epiclastic rocks in the upper part sequence. *Basalt to trachybasalt lava with subordinate basaltic pyroclastic deposits* are the oldest Cenozoic volcanic rocks exposed in the area. These volcanic and volcanoclastic rocks, generally referred to as the Amaro and Gamo basalts, were originally attributed to an early phase of Afar-related volcanism (Stewart and Rogers, 1996). The sequence is mainly alternating up to 3 m thick massive lava flows with slightly to strongly weathered surfaces. They consist of plagioclase, clinopyroxene and olivine. Dominant basalts to trachybasalts are massive, dark-colored rocks with columnar jointing. Lava flows consists autoclastic breccia of highly fractured and angular clasts and volcanoclastic deposits (Figure 21) classified as matrix-supported to clast-supported agglomerate and lapilli stone surrounded by amygdaloidal basalts. *Rhyolitic ignimbrite with subordinate rhyolite lava* exposed on steep slopes of an escarpment on the plateau. Rhyolite lava flows and small domes are spatially related to a strongly welded crystal-rich ignimbrite, locally having fluidal texture and rheomorphic deformation. Columnar jointing locally occurs in moderately to densely welded

ignimbrites. **Trachyte to trachybasalt lava** forms strongly weathered lava flows and volcanic necks mainly in the northern part of the area. Light gray to gray trachytes and dark gray trachyandesite are fine-grained, porphyritic rocks with trachytic texture (Figure 20).



Figure 20. The field photograph of highly altered trachyte to trachybasalt showing porphyritic texture. Road-cut east of Geresse.



Figure 21. The field photograph of basalt to trachybasalt lava with subordinate basaltic pyroclastic deposits (called as the Amaro-Gamo basalt; Stewart and Rogers, 1996). Road-cut east of Geresse.

Early-Rift volcanic lava flow and volcanoclastic deposits (Pliocene-Miocene)

Alkali basalt to trachybasalt lava and basaltic volcanoclastic deposits are dominantly dark colored alkali basalts, with well-developed columnar joints intercalated with paleosol horizons and fine basaltic scoria layers (thick up to 2 m). Brownish to reddish crusts are typical of partly weathered basalts. It commonly made by olivine, plagioclase and clinopyroxene. **Rhyolite lava with subordinate volcanic breccia and ignimbrite** form small lava flows, lava domes, volcanic necks and ignimbrite layers at western part of the area. Light gray to red flow banded rhyolites are porphyritic or aphanitic rocks. It is composed of quartz, K-feldspar and also rare clinopyroxene or amphibole. The predominant welded yellowish rhyolitic to trachytic ignimbrite reveals various content of fiamme. Massive perlites to glassy ignimbrites with relics of petrified wood are preserved along the weathered surface. **Trachyte to trachybasalt** forms dykes that predominant unit shows light gray, fine grained trachyte with aphanitic or porphyritic texture. The trachybasalts are subordinate and have dark gray color, massive, and porphyritic in texture. The most common composition is plagioclase and clinopyroxene. Dykes are often

moderately to highly altered (argillitization) and sharp contact with the host rock. ***Trachyte with subordinate trachyte volcanoclastic deposits*** form volcanic plugs and dykes as well as small lava flows. They consist of hydrothermally altered blocks, volcanic bombs and angular trachyte clasts in a matrix of ash. Light gray trachyte is a fine-grained rock with aphanitic to porphyritic texture formed mainly by K-feldspar crystals. ***Rhyolitic ignimbrite with subordinate pyroclastic fall deposits*** exposed around Arbe Gona and Bursa. Individual bluish-gray to white ignimbrite layers, locally with columnar jointing, vary from less than 1 to 8 m in thickness. The most common volcanic lithofacies include welded ignimbrite with varying amounts of fiamme and feldspar crystals.

Quaternary Sediments (Pleistocene to Holocene)

The youngest lithologies are different types of quaternary sediments such as colluvial sediments, lacustrine sediments, alluvial deposits and fluvial sediments of different grain size covering the study area as listed below.

Colluvial sediments represented mainly by accumulations of sediments composed of a wide range of non-cohesive of various grain sizes. The sediments are mostly unsorted, matrix-supported, with angular to subangular shaped cobbles and boulders. ***Polygenetic sediments (volcanoclastic alluvial and lacustrine sediments)*** are associated sedimentary infills of varying origin and lithology formed by alternation of coarser grained clastic alluvial sediments at depressions laterally grading into finer grained predominantly clayey to silty lacustrine sediments with higher organic matter content. ***Colluvial to alluvial sediments*** forms accumulations of non-active alluvial fans located in the foothills of scarps characterized by alternating coarse grained cobbles to boulders of colluvium of debris cone deposits with gravel and sandy. ***Alluvial fan deposits*** are preserved as accumulations of older phases of outwash cones exposed to erosion processes. ***Fluvial sediments*** deposits associated with river channels and floodplains. The character of the sediments depends on the fluvial style and source material in the river basin infilled by migrated sand and gravel.

6. Tectonics

In this chapter, the overall field structural and tectonic pattern belonging to the southwestern Gamo Zone (Hammar Domain) and southeastern Sidama Region (Adola-Moyale Belt) which both overlie the sequence of pre- to early-rift volcanites and volcanoclastic deposits of the Main Ethiopian Rift is described.

6.1. Neoproterozoic rocks of the Hammar Domain and Adola-Moyale Belt

The studied Neoproterozoic rocks of the Hammar Domain and Adola-Moyale Belt (Southern Ethiopian Shield) cropping out in deep erosional valleys. They are mainly represented by medium to high-grade rock assemblage (e.g. amphibolites, paragneisses, migmatites and orthogneisses) with occurrence of small granite to diorite intrusions (e.g. Verner et al. 2021 and references therein). In these rocks the sequence of metamorphic and magmatic fabrics such as compositional banding, schistosity or metamorphic and magmatic foliation were identified. In addition, the brittle structures (normal to oblique-slip faults and extensional joints) significantly affected the overall geological and geomorphological pattern of the mapped areas (Figure 22 & Figure 27).

Northwestern Hammar Domain (Gamo Zone)

In the medium to high-grade rocks of the northwestern Hammar Domain (Figure 22), three distinct regional metamorphic foliations were identified. The relics of flat-lying or gently dipping compositional banding (S_1) form asymmetric, often tight to isoclinal folds of various scales (Figure 23c, d) within a younger regional metamorphic foliation (S_2). Corresponding fold axes plunge gently to the ~NNW or ~SSE. In some places, steeply ~WSW or ~ENE dipping axial cleavage, mostly parallel to the new regional foliation S_2 , was identified. Superimposed foliation S_2 (Figure 23b, c, d and 25a) dips steeply to ~SW(WSW) or ~NE(ENE) bearing gently ~NW(SE) plunging stretching or mineral lineation (Figure 24a). In the regional scale, the foliation S_2 defines main lithological boundaries between individual rock types as well as overall tectonic pattern of mapped exposure of the Hammar Domain (Figure 23a).

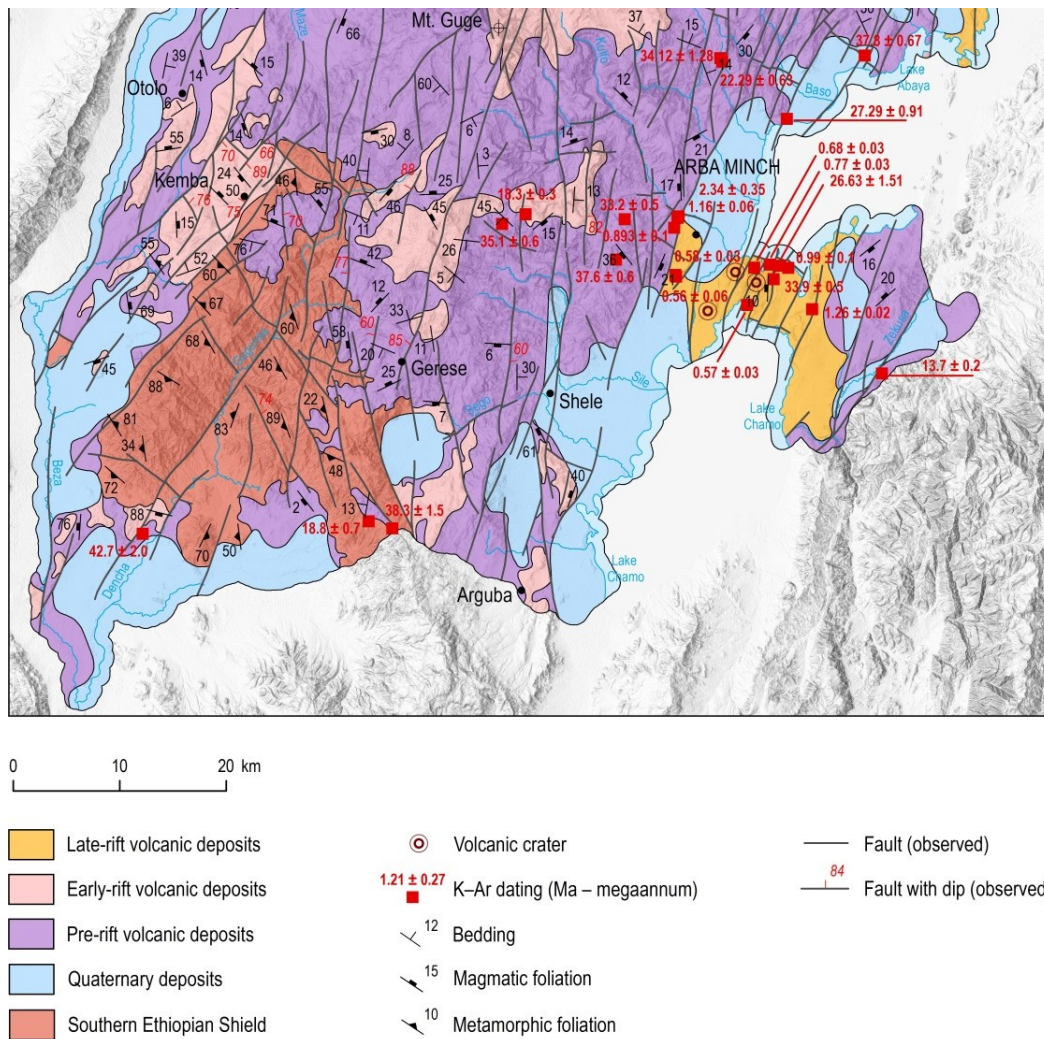


Figure 22. Schematic structural map of the southernmost part of the Hammar Domain and overlying volcanic and volcanoclastic sequences of the Main Ethiopian Rift.

The foliations S_1 and S_2 in all the lithologies were heterogeneously refolded into a younger foliation S_3 (Figure 24a). The axial plane, associated axial cleavage (Figure 25b and Figure 26b) and/or penetrative foliation S_3 dip gently to the ~SW to WSW (Figure 24b).

Numerous granites to granodiorite intrusions reveal an intrusive, steeply dipping, NW(NNW)–SE(SSE) trending contacts, mostly parallel to the regional foliation S_2 . The presence of mafic microgranular enclaves (MME) within the granite sheets reveal an evidence of magma mingling among individual diorite, leucogranite and host granite magma (Figure 26a). In addition, the zones of transitional, magmatic to solid-state overprint and partial recrystallization parallel to foliation S_2 were identified (Figure 26a). The early generation of superimposed narrow ductile to brittle-ductile shear or mylonite zones (up to 2 meters in width) is often accompanied by abundant hydrothermal mineralization dipping steeply to the

~SW(SSW). The associated lineation plunges gently to the ~SSW with prevailing left-lateral kinematics. The relatively younger narrow shear zones and faults dip steeply to moderately to the ~NW or gently to the ~SSW. The abundant quartz and quartz-tourmaline veins were systematically observed in two distinct orientation (Figure 24c): (a) The first group includes the dikes or veins (up to 3 meters thick) dip steeply to the W(WNW) or E(ESE). (b) The second group consists of quartz or aplite veins (up to ca. 0.2 meters in thickness) revealing discordant contacts dipping steeply to the ~S.

A discontinuous, few decimeters to about 2 meters thick, layer of conglomerate mainly comprised of quartz pebbles form non-conformity overlying the sequences of metamorphic rocks of the Hammar Domain (Figure 23a).

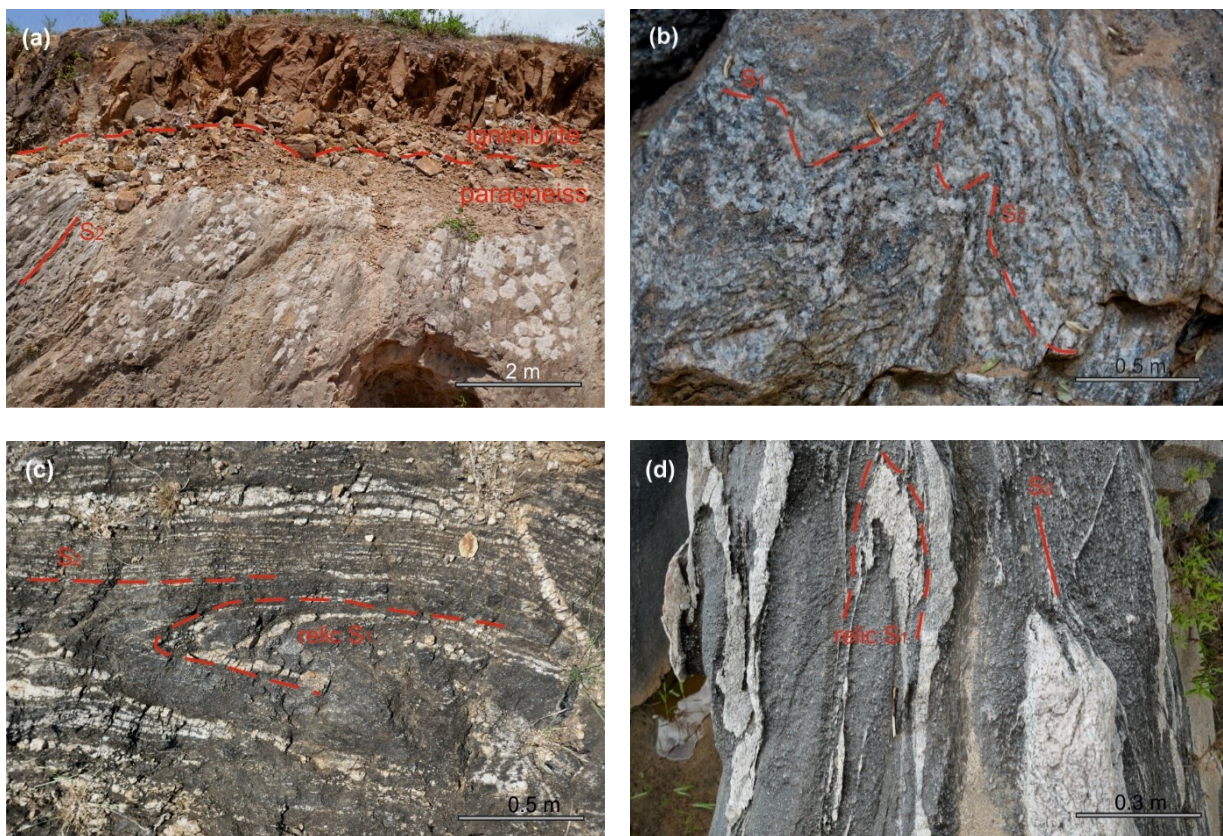


Figure 23. Examples of outcrops on the road-cut south of Gerese town. (a) Layer of conglomerate with few decimeters to 2 meters thickness including mainly quartz pebbles and rift-related volcanic or volcanoclastic rocks overlying the sequences of metamorphic rocks of the Hammar Unit. (b) Relict folds of the oldest flat-lying or gently dipping compositional banding (S_1). (c) Tight to isoclinal folds of various scales within a younger regional metamorphic foliation (S_2). (d) Isoclinal folds of melts in amphibolites within a younger regional metamorphic foliation (S_2).

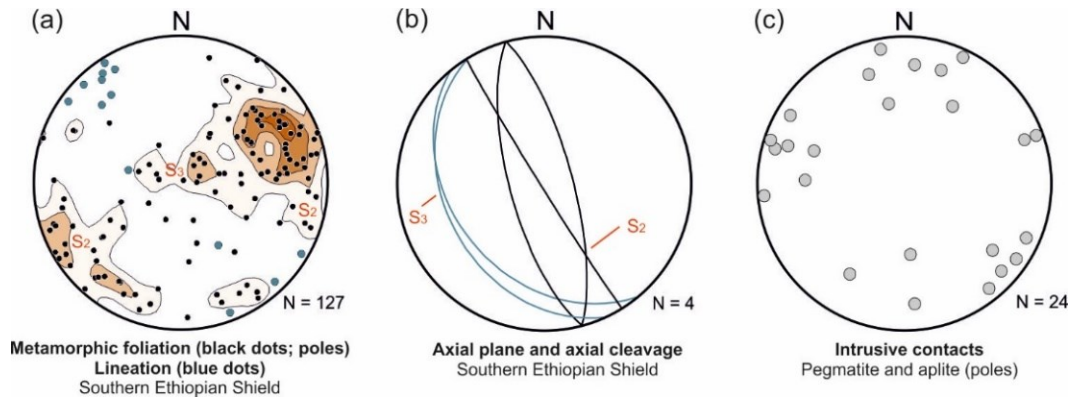


Figure 24. Orientation diagrams (equal projection to the lower hemisphere): (a) Metamorphic foliation S_2 and S_3 (black dots; poles) and associated stretching or mineral lineation (blue dots); (b) Axial plane and axial cleavage S_2 and S_3 ; (c) Intrusive contacts of aplite and pegmatite dikes.

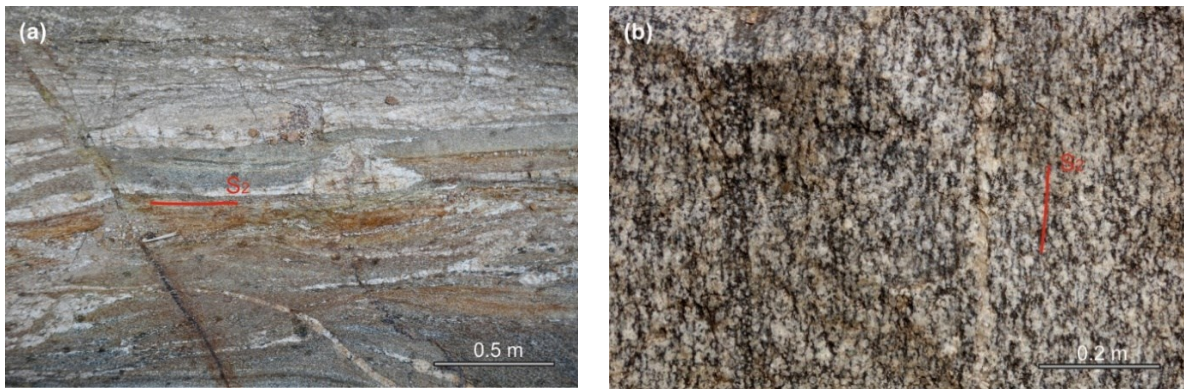


Figure 25. Mesoscopic photographs of: (a) Penetrative metamorphic foliation S_2 in various outcrops foliation defined by irregular compositional banding dipping steeply to SW, a road-cut east of Kemba town. (b) Superimposed metamorphic foliation S_3 in biotite orthogneiss, a road-cut south of Geresse.

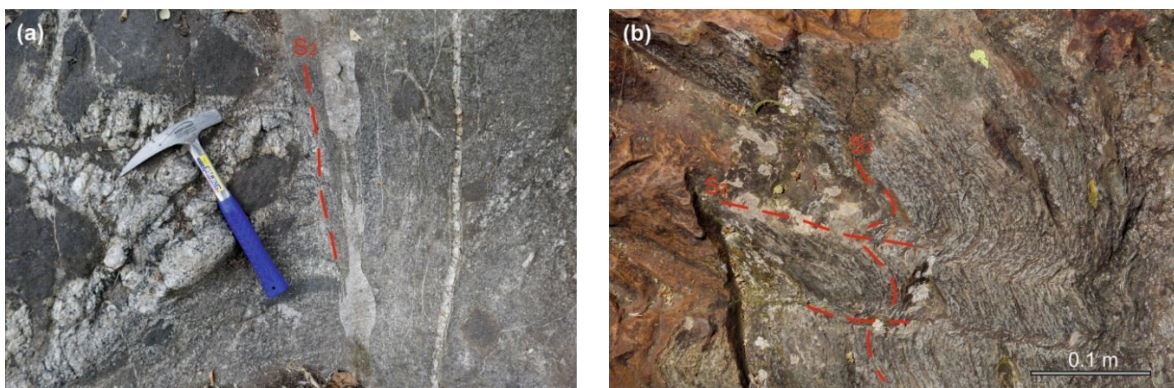


Figure 26. Mesoscopic photographs of: (a) The structures formed by magma mingling between diorite melt (MME) and leucogranite, overprinting by solid-state deformation and recrystallization (regional S_2 foliation), a river bed south of Geresse. (b) Asymmetrically folded regional S_2 fabric to gently W-dipping foliation, locally forming kink band structures and axial cleavage S_3 , on a road-cut south of Geresse town.

Northwestern Adola-Moyale Belt

In the northwestern Adola-Moyale Belt the relics of the oldest flat-lying compositional banding (S_1) form partly asymmetric, often tight to isoclinal folds plunging gently to $\sim N$ or S , corresponding axial plane of $N(NNE)$ – $S(SSW)$. At the regional scale, superimposed foliation S_2 dips steeply to $\sim W(WNW)$ or $\sim E(ESE)$ (Figure 30a). The foliation S_2 is associated with stretching or mineral lineation plunging gently to N or S . The set of S_1 and S_2 fabrics in all the lithologies were heterogeneously refolded into a younger foliation S_3 dipping shallowly to the $\sim W$ to WNW (Figure 30a and Figure 28). Well-developed stretching lineation plunging gently to $\sim NW$ was observed (Figure 30b).

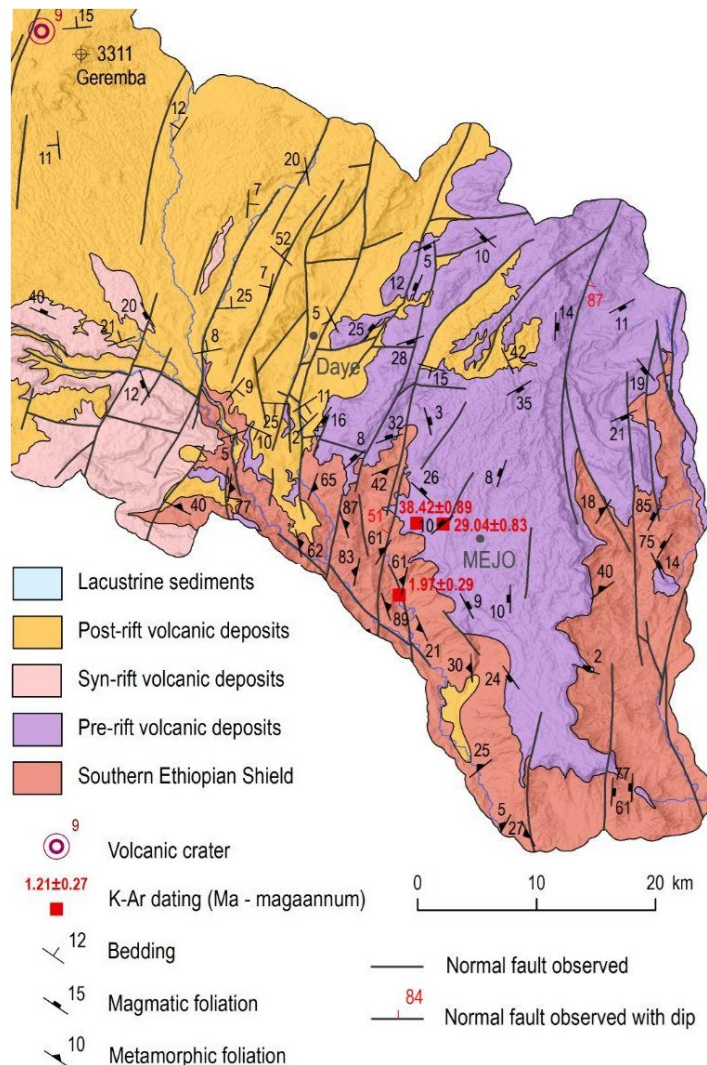


Figure 27. Simplified tectonic map of the Sidama Region showing a regional fabric pattern and mapped faults.

Early generation of superimposed narrow ductile to brittle-ductile shear or mylonite zones (up to 2 meters in width) is often accompanied by abundant hydrothermal mineralization dipping steeply to ~E. Associated lineation plunges steeply or moderately to ~SSW with prevailing oblique slip right-lateral kinematics. The relatively younger narrow shear zones and faults dip steeply to moderately to ~NW or gently to ~SSW. The abundant quartz veins (up to 0.8 meter in thickness) were systematically observed (Figure 29) showing discordant contacts dipping steeply ~NW(NNW).



Figure 28. Younger foliation S_3 in biotite orthogneisses dipping shallowly to the ~W to WNW. South of Girja village.



Figure 29. Quartz vein with discordant contacts dipping steeply to ~NW(NNW).

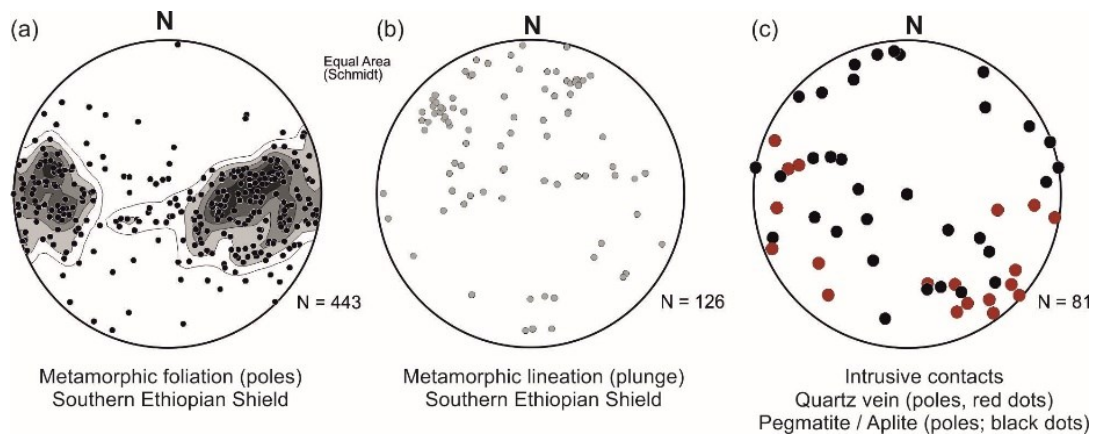


Figure 30. Orientation diagrams: (a) Metamorphic foliation (poles); (b) mineral lineation (plunge).

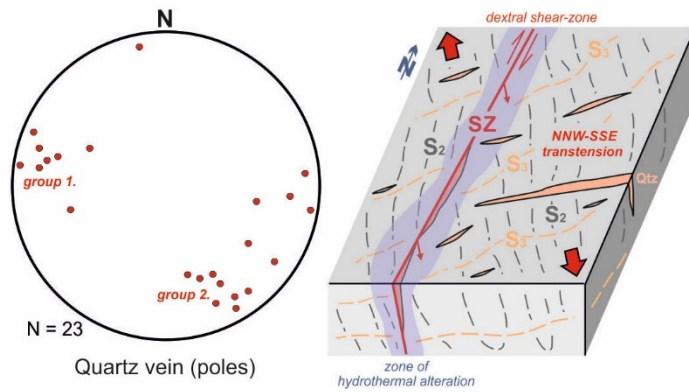


Figure 31. Equal projection to the lower hemisphere diagram showing the orientation of intrusive contacts of quartz veins and schematic block diagram of hydrothermal quartz vein and regional N-S trending shear zone.

6.2. Fabric pattern in overlying volcanic rocks and volcanoclastic deposits (MER)

The volcanic and volcano-sedimentary fabrics in rift-related rocks reveal the planar preferred orientation of rock-forming minerals, micro-vesicles or microcrystals and elongated mineral grains, lithic fragments or stretched and welded pumice fragments (Figure 33b). The flow foliation in volcanic rocks as well as the bedding planes (S_0) in welded ignimbrites and other volcanoclastic deposits of pre-rift and early-rift formations exhibit a wider orientation maximum reflecting, sub-horizontal, \sim NW or \sim SE(ESE) gently dipping planes (Figure 32a, b). The bedding planes (S_0) in welded ignimbrites correspond to flow-stretching of viscous silicic lava or hot glass fragments during the flow. Associated weakly developed mineral lineation and linear elongation of fragments plunge gently to \sim E(ESE) or \sim W(WNW). The bedding planes (S_0) in welded or unwelded ignimbrites and other volcanoclastic deposits belonging to late-rift formations, with the exception of individual volcanoes or isolated cinder cones, exhibit scarce bedding mainly in the sub-horizontal orientation (Figure 32a, b). In some places, the original lithological boundaries, contacts of the lava flow and the primary fabric, were modified by rift-related normal faulting or locally by rock falls or landslides.

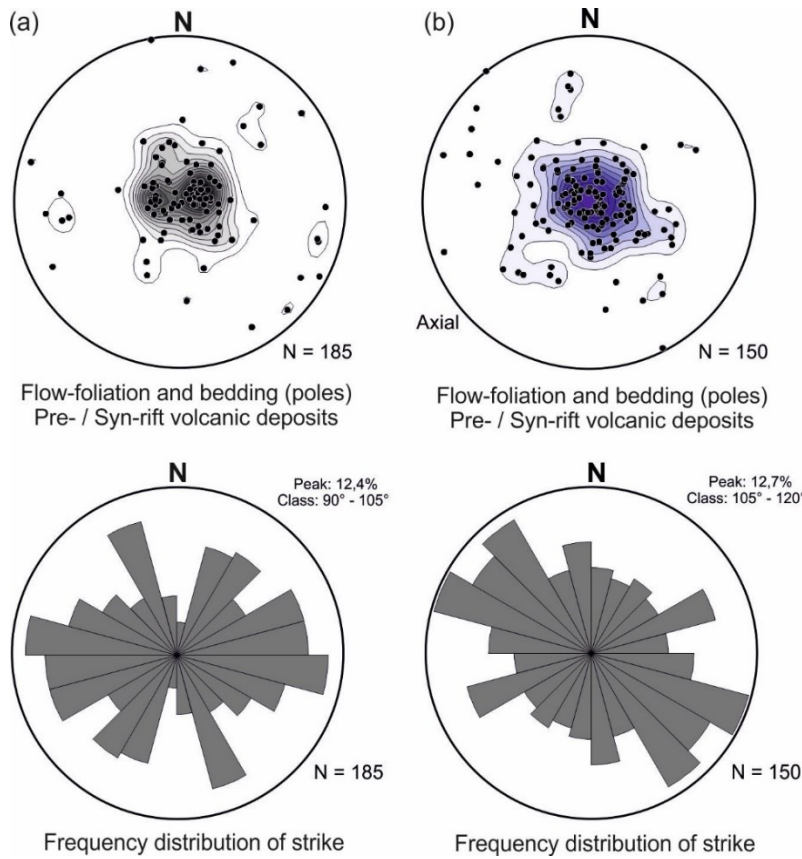


Figure 32. Orientation diagrams of the primary structures in volcanic and volcanoclastic sequences: (a) Flow foliation and bedding planes (poles) in the pre-rift to early-rift volcanoclastic rocks deposits and frequency distribution of strike (southeastern Sidama Region). (b) Flow foliation and bedding planes (poles) in the pre-rift to early-rift volcanoclastic rocks deposits and frequency distribution of strike (southern Gamo Zone).

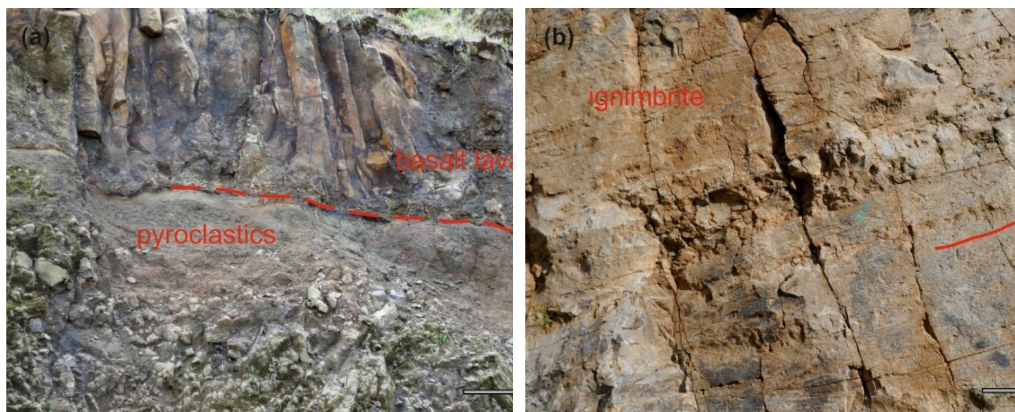


Figure 33. (a) Early-rift basalt lava flow with well-developed columnar jointing (upper part) overlying ash-fall pyroclastic deposits (lower part), the road-cut 2 km west of Shele. (b) Bedding plane (So) in rhyolite ignimbrite defined by elongated mineral grains, lithic fragments (stretched and welded pumice fragment), on the road-cut 3 km north of Lante.

6.3. Brittle Structures

Faults and fault zones

Across the mapped area, several sets of brittle structures (e.g. normal faults to oblique-slip faults and fault zones, and extensional joints) were observed (Figure 34). Regional faults and fault zones related to the Main Ethiopian Rift significantly affect the geological framework of the area and are mostly parallel with the NNE(N) to SSW(S) oriented axis of the rift and morphological escarpments. A subordinate set of normal faults has a ~E–W trend (Figure 34a).

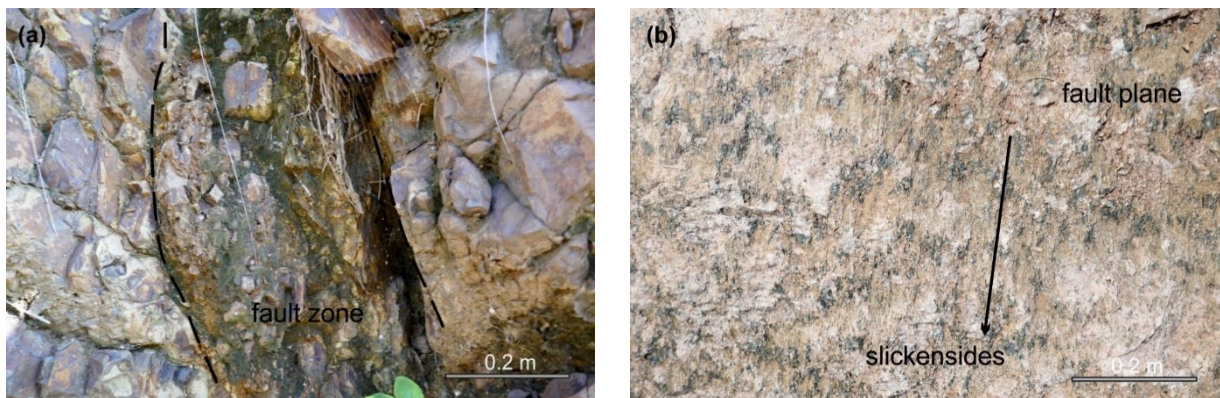


Figure 34. N–S trending rift-related faults in medium-grade rocks of the Hammar Domain, a road-cut South of Geresse. (b) The fault plane with steeply plunging slickensides and indicators of normal kinematics, a road-cut South of Geresse.

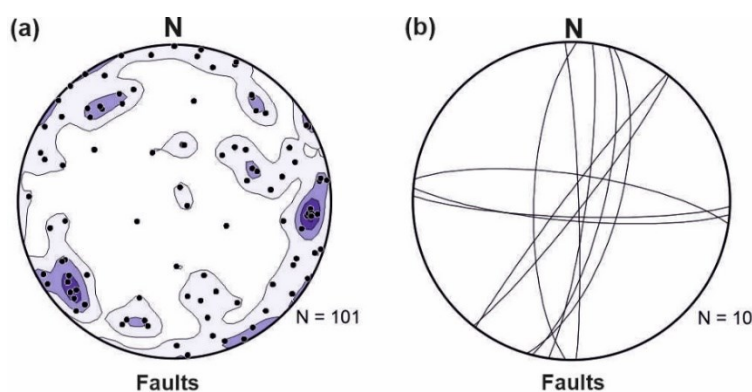


Figure 35. (a) Orientation diagrams of faults / fault zones (poles) in southern Gamo zone (Hammar Domain and overlying volcanites of Main Ethiopian Rift); (b) Orientation diagrams of faults / fault zones (arcs) in southeastern Sidama Region (Adola-Moyale Belt) and overlying volcanites of Main Ethiopian Rift.

Moreover, minor oblique- to strike-slip faults with both left- and right-lateral kinematic indicators were mapped as subordinate shear joints or minor faults (e.g. Figure 34b). The orientation of faults in individual directions is shown on the rose diagram (Figure 35a). The occurrence of faults in the SES is more variable, mostly reflecting the superposition of the prominent rift-related faults described above and the relatively older fault structures that were active in the “pre-rift” episode.

Extensional joints

Extensional joints occur in three distinct sets with a similar direction frequency. Across all the lithological units built by volcanoclastic rocks, extensional joints trend ~N(NNE)–S(SSW) or W(WNW)–E(ESE) (Figure 34b). Their orientation is largely consistent with regional faults of the Main Ethiopian Rift. Extensional joints in medium to high-grade rocks generation are mostly steep, trending ~E(WNW)–W(ESE), as shown in the Figure 36a, b.

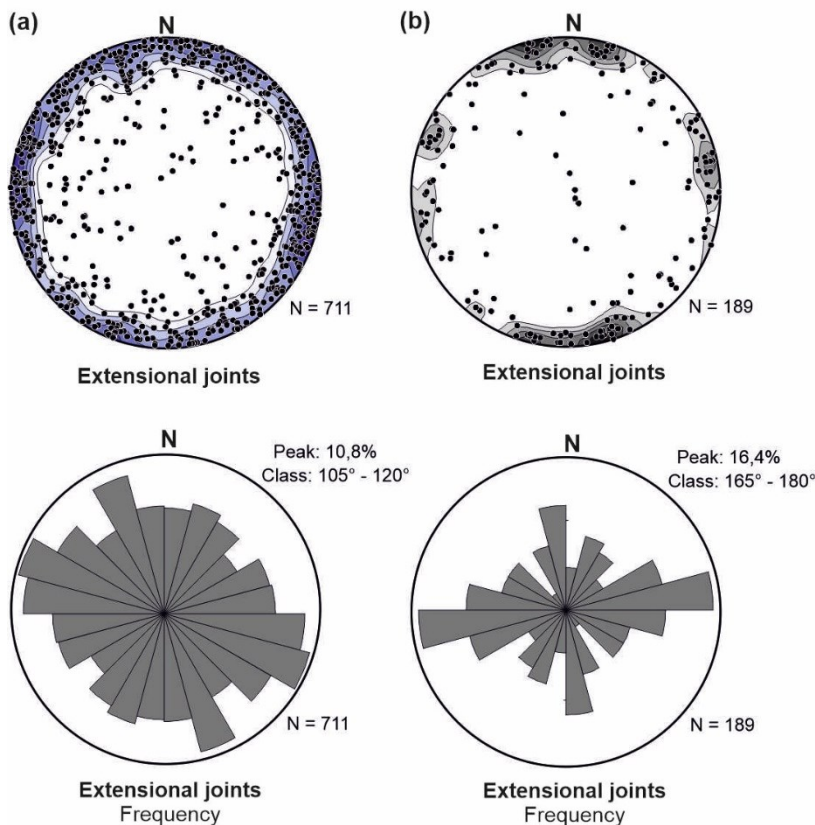


Figure 36. Orientation diagrams of extensional joints in southern Gamo zone (Hammar Domain and overlying volcanites of Main Ethiopian Rift) and frequency in individual directions; (b) Orientation diagrams of extensional joints in southeastern Sidama Region (Adola-Moyale Belt) and overlying volcanites of Main Ethiopian Rift) and frequency in individual directions.

7. U-Pb Dating

The high-grade biotite to amphibole-biotite orthogneiss the southern Hammar Domain (Southern Ethiopian Shield), coordinates: 5.8871028N, 37.2802669E (southwest of Geresse) was dated using the U/Pb method on zircons by Laser Ablation ICP–MS method. A criterion of discordance was chosen that is $> 1\%$ and the uncertainties of the analyses used for interpretation at the 2σ level and Concordia age was plotted with the mean squared weighted deviation (MSWD) and the probability of concordance (for more information see Annex 3).

This rock gives an age of about 773.2 ± 5.8 Ma on concordia plot. Based on zircon structure reveals magmatic zoning the age is interpreted as the crystallization age of granite protolith. There is some indication that shows the heterogeneity of zircon grains dated as older than 900 Ma on concordia plot (Figure 37). According to Yibas et al. (2000), U–Pb zircon geochronological studies suggested that the Precambrian of southern ANS in Ethiopia is dominated by granitoids and orthogneisses emplaced between 900 and 550 Ma. According to Fritz et al. (2013) the U–Pb data from the high-grade rocks which are interpreted as an inherited component derived from igneous or volcano-sedimentary protolith, do not exceed 780 Ma. This suggest that the Southern Ethiopian Shield has a juvenile origin far away from cratonic sources and might have been derived from a volcano-sedimentary intra-oceanic magmatic arc in the early stage of EAO.

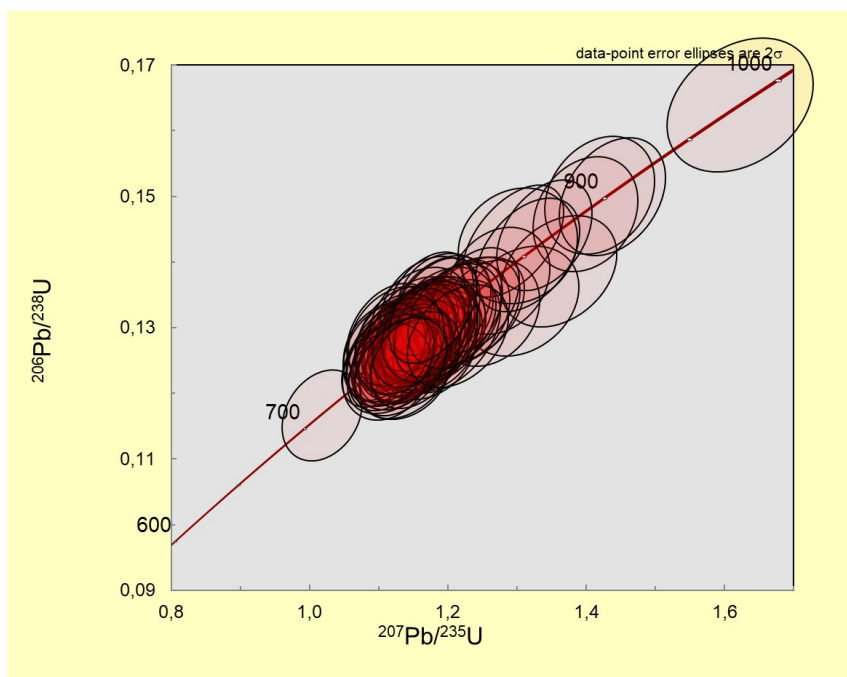


Figure 37. Concordia Age = 773.2 ± 5.8 Ma (2σ , decay-const. errs included) MSWD of concordance = 1.13, Probability of concordance = 0.29.

8. Geological map compilation

As part of this work, the geological map of the northern Hammar Domain (Annex 1) and the northwestern part of the Adola-Moyale Belt (Annex 2) was compiled, including an interpretive geological section. These map outputs summarize a detailed geological documentation, knowledge of structural evolution, overall lithological pattern considering the stratigraphic framework with regard to the relationships among an individual lithologies and available geochronological data.

The geological map of the southwestern Gamo Zone (Hammar Domain and overlying volcanites of MER; Annex 1) includes a complex of highly metamorphosed rocks (e.g. amphibolites, migmatites, paragneisses and orthogneisses) which were intruded by several granitic bodies. Most of high-grade metamorphic lithologies reveal a NW(N)–SE(S) trending S_2 foliation-parallel boundaries. These rocks crop out in the deeper parts of erosional valleys. These high-grade rocks are overlain by almost flat-lying volcanic and volcanoclastic sequences belonging to the Main Ethiopian Rift. The superimposed normal to oblique-slip faults are mostly parallel to the morphological escarpments reflecting the continental rifting in Cenozoic to recent era.

The geological map of the southeastern Sidama Region (northern tip of the Adola-Moyale Belt and overlying volcanites of MER; Annex 2) is mainly composed of medium -grade orthogneisses, amphibolites and schists and Cenozoic rift-related volcanic and volcanoclastic deposits on the top. The metamorphic rocks show a lithological boundary parallel to prevailing NNE(N) to SSW(S) trending foliation dipping steeply to moderately direction which has been heterogeneously transposed into flat-lying directions. The Cenozoic rift-related sequences have a discordant contact, mostly in sub-horizontal orientation. On some places, the original lithological boundaries were modified by principal N(NNE)-S(SSW) and subordinate E-W trending normal faults.

9. Discussion

The studied area is built by high-grade rock assemblage of Neoproterozoic age belonging to the northern Hammar Domain and Adola-Moyale Belt in Southern Ethiopian Shield (SES). These rocks are overlain by the Cenozoic lava flows and volcanoclastic deposits of the Main Ethiopian Rift (MER).

The results of morphotectonic analysis of the Digital Elevation Model from both areas of interest mostly represent Cenozoic faults and/or main lithological boundaries. The relics of flat-lying or gently dipping compositional banding (S_1) in a form of asymmetric, tight to isoclinal folds are enclosed in the regional metamorphic foliation (S_2). The regional foliation S_2 dip steeply to moderately to ~E or W (in the northern tip of the Adola-Moyale Belt) and to ~ENE(NE) or WSW(SW) in the northern part of the Hammar Domain. Largely superimposed gently ~NW dipping foliation S_3 with well-developed stretching lineation plunging to ~NW is more intensively developed in the northern part of the Adola-Moyale Belt. The localized tectonic activity was associated with the origin of regional brittle to brittle-ductile N(NW) – S(SE) trending strike-slip shear zones, with predominant sinistral kinematics. The hydrothermal mineralization with the presence of abundant quartz-rich veins closely associated with these deformation zones. As part of this thesis, the age of the biotitic orthogneiss of the Hammar Domain was determined at 773.2 ± 5.8 Ma revealing the magmatic (crystallization) age of granite protolith.

The previous geochronological studies from wider SES region (e.g. Ayalew and Johnson, 2002; Woldemichael et al., 2010; Yibas et al. 2000; Verner et al. 2021) suggest that the crystallization age of biotitic orthogneiss protolith (773.2 ± 5.8 Ma) fits well to period of subduction of Megado oceanic crust and formation of volcanic (magmatic) arc(s) at ca. 830–750 Ma. This fact also suggests that the Southern Ethiopian Shield has a juvenile origin far away from Cratonic sources and might have been derived from a volcano-sedimentary intra-oceanic magmatic arc in the early stage of EAO.

This fabric pattern fits well to deformational events (D_1 to D_3) that have been established by Tolessa et al. (1991) and Bonavia and Chorowic (1993), Ghebreab et al. (1992); Worku and Schandelmeier (1996), Tsige and Abdelsalam (2005) and Verner et al. (2021). The early deformational event D_1 could be linked with the early accretion of island arcs commenced

between 750 and 650 Ma called as the “Megado Event” (Woldemichael et al. 2010; Stern et al. 2012 and references therein) or with the episode of high-grade metamorphism and anatexis in the time-span ca. 750 to 700 Ma (Verner et al. 2021).

In the regional scale, the intense superimposition of steeply dipping foliation S_2 (D_2 event) was formed due to ~E–W oriented horizontal shortening (compression). These fabrics define the main lithological boundaries between individual rock types as well as overall tectonic pattern of mapped exposure of the Hammar Domain and the Adola-Moyale Belt. These processes were mostly associated with the “Moyale Tectonothermal Event” (dated at ca. 660 Ma) and/or with the “Late Cryogeanian-Ediacaran-Cambrian Pan-African episode” at ca. 650–620 Ma closely related to the continental collision between East Gondwana and the consolidated Congo-Tanzanian-Saharan Craton (West Gondwana) as previously defined by Teklay et al. (1998), Yibas et al. (2002), Stern et al. (2012) and Verner et al. (2021). The latter processes of superimposition of flat- to gently dipping foliation S_3 were associated with subvertical shortening due to the late-orogenic crustal exhumation well-recorded in the Adola-Moyale Belt (e.g. Yihunie and Tesfaye, 2002), roughly coeval with an early ductile NW-SE trending shear zones (the record of left-lateral transpression) according to Verner et al. (2021). These sinistral strike-slip shear zones in N–S and NW–SE orientations are interpreted as antithetic Riedel Shears (Worku and Schandelmeier, 1996).

Minor differences in the orientation maxima of the regional S_2 foliation in the Hammar Domain and Adola-Moyale Belt are mostly due to the variable intensity of superposition of both exhumation-related S_3 structures and localized shear zones.

The main tectonothermal events and magmatic episodes (e.g. Teklay et al., 1998; Yibas et al., 2002 and Stern et al., 2012; Verner et al. 2021 and this thesis), similarly for both areas of our interest, could be summarized as follows: as: (a) the “Megado Tectonothermal Event” (ca. 770–700 Ma) both of which are associated with volcanic arc formation and emplacement granite protolith of abundant orthogneisses, followed by (b) the “Moyale Tectonothermal Event” (ca. 660 Ma) associated with main collisional episode between East Gondwana and the consolidated Congo–Tanzanian–Saharan craton of West Gondwana and (c) Ediacaran–Cambrian Pan-African episode (ca. 630–500 Ma) mainly linked with the late-orogenic exhumation, post-orogenic magmatism and localized activity along the regional strike-slip shear zones.

10. Conclusions

Based on detailed field geological mapping, morphotectonic analysis of Digital Elevation Model, detailed structural analysis and U/Pb dating results of biotite orthogneiss from the Hammar Domain the overall tectonic evolution associated with the East-African Orogeny is interpreted.

The structural evolution of the northern Hammar Domain and northwestern tip of the Adola-Moyale Belt could be defined into four deformation phases D_1 to D_4 resulted in origin of: (a) Relict compositional banding (S_1) of flat-lying orientation defining the primary contacts of high- to medium grade lithologies, (b) superimposed steeply to moderately dipping $\sim N-S$ to $\sim NW-SE$ trending compressional foliation (S_2) due to a regional $\sim E-W$ oriented compression and (c) later sub-horizontal to gently $\sim NW$ dipping foliation (S_3) associated with well-developed NW plunging lineation. Furthermore, the localized tectonic activity was concentrated in the form of narrow brittle-ductile to brittle $\sim N-S$ to $\sim NW-SE$ trending shear zones, commonly accompanied by hydrothermal mineralization.

New geochronological data from biotite orthogneiss yielded at 773.2 ± 5.8 Ma reveal the magmatic (crystallization) age of granite protolith. The rock assemblage has been affected by polyphase deformation and recrystallization due to main collisional event and exhumation at ca. 660 Ma which corresponds to Gondwana continent assembly.

The overall geodynamic scenario could be summarized as follows: (a) the “Megado Tectonothermal Event” (ca. 770–700 Ma) roughly associated with volcanic arc formation and emplacement granite protolith of abundant orthogneisses, followed by (b) the “Moyale Tectonothermal Event” (ca. 660 Ma) associated with main collisional episode between East Gondwana and the consolidated Congo–Tanzanian–Saharan craton of West Gondwana and (c) Ediacaran–Cambrian Pan–African episode (ca. 630–500 Ma) mainly linked with the late-orogenic exhumation, post-orogenic magmatism and localized activity along the regional strike-slip shear zones.

List of References:

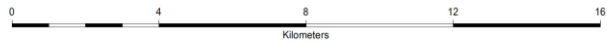
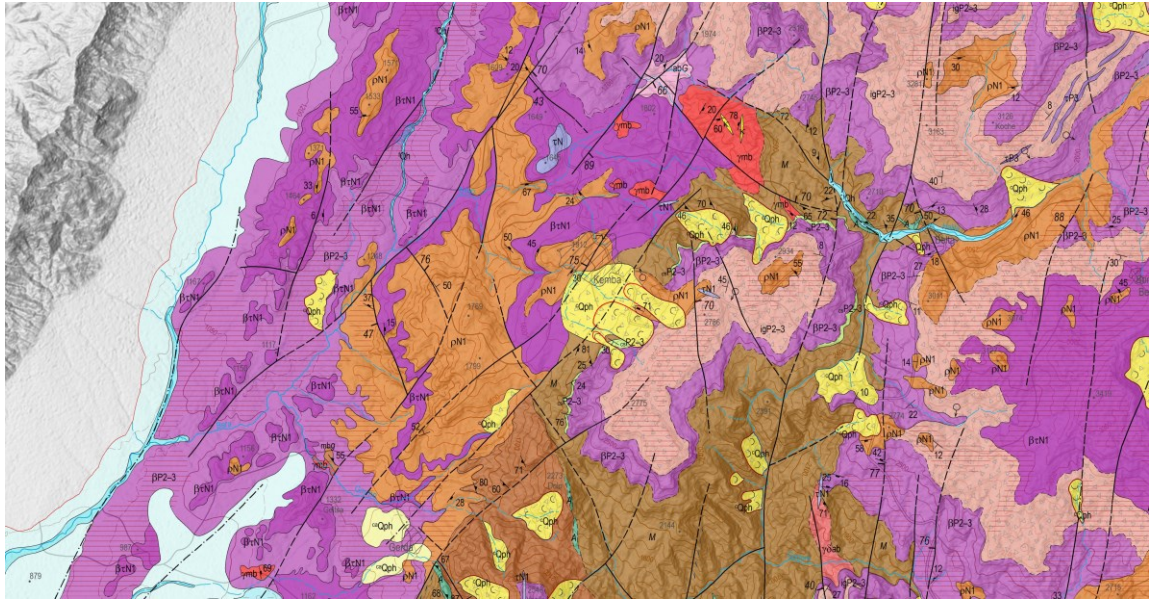
- Abdelsalam, M.G., Stern, R.J., (1996). *Sutures and shear zones in the Arabian–Nubian Shield. Journal of African Earth Sciences*, 23(3), 289–310.
- Alemu, T., Abebe, T., 2007. *Geology and tectonic evolution of the Pan–African Tulu Dimtu Belt, Western Ethiopia. Online Journal of Earth Sciences* 1 (1), 24–42.
- Alene, M., Barker, A.J., 1993. *Tectonometamorphic evolution of the Moyale region, southern Ethiopia. Precambr. Res.* 62 (3), 271–283.
- Allen, A., Tadesse, G., 2003. *Geological setting and tectonic subdivision of the Neoproterozoic orogenic belt of Tulu Dimtu, western Ethiopia. J. Afr. Earth Sc.* 36 (4), 329–343.
- Asrat, A., Barbey, P., Gleizes, G., 2001. *The Precambrian geology of Ethiopia: a review. Africa Geoscience Review* 8 (3/4), 271–288.
- Asrat, A., Barbey, P., 2003. *Petrology, geochronology and Sr–Nd isotopic geochemistry of the Konso pluton, south–western Ethiopia: implications for transition from convergence to extension in the Mozambique Belt. Int. J. Earth Sci.* 92 (6), 873–890.
- Avigad, D., Stern, R.J., Beyth, M., Miller, N., McWilliams, M.O., 2007. *Detrital zircon U–Pb geochronology of Cryogenian diamictites and Lower Paleozoic sandstone in Ethiopia (Tigray): age constraints on Neoproterozoic glaciation and crustal evolution of the southern Arabian Nubian Shield. Precambrian Research*, 154(1–2), 88–106.
- Avigad, D., 2007. *Late Neoproterozoic rise and fall of the northern Arabian–Nubian shield: The role of lithospheric mantle delamination and subsequent thermal subsidence. Tectonophysics* 477(3):217–228.
- Ayalew, T., Bell, K., Moore, J.M., Parrish, R.R., 1990. *U–Pb and Rb–Sr geochronology of the western Ethiopian shield. Geol. Soc. Am. Bull.* 102 (9), 1309–1316.
- Ayalew, T., Johnson, T.E., 2002. *The geotectonic evolution of the Western Ethiopian shield. SINET: Ethiopian Journal of Science* 25 (2), 227–252.
- Blades, M.L., Collins, A.S., Foden, J., Payne, J.L., Xu, X., Alemu, T., Woldetinsae, G., Clark, C., Taylor, R.J., 2015. *Age and hafnium isotopic evolution of the Didesa and Kemashi Domains, western Ethiopia. Precambr. Res.* 270, 267–284.
- Bonavia, F.F., Chorowicz, J., 1992. *Northward expulsion of the Pan–African of northeast Africa guided by a reentrant zone of the Tanzania craton. Geology* 20 (11), 1023–1026.
- Bowden, S., Gani, N.D., Alemu, T., O’Sullivan, P., Abebe, B., Tadesse, K., 2020. *Evolution of the Western Ethiopian Shield revealed through U–Pb geochronology, petrogenesis, and geochemistry of syn–and post–tectonic intrusive rocks. Precambr. Res.* 338, 105588.
- Davidson, A., 1983. *The Omo River project: reconnaissance geology and geochemistry of parts of Illubabor, Kefa, Gemu and Sidamo. Ethiopia, Bulletin Ethiopian Institute of Geological Surveys, Ministry of Mines and Energy*, p. 2.

- de Wit, M.J., Chewaka, S., 1981. Plate tectonic evolution of Ethiopia and the origin of its mineral deposits: an overview. In: Chewaka S, de Wit MJ (eds) Plate tectonics and metallogenesis: some guidelines to Ethiopian mineral deposits. *Ethiopian Inst Geol Surv Bull* 2:115–129.
- Fritz, H., Abdelsalam, M., Ali, K.A., Bingen, B., Collins, A.S., Fowler, A.R., Ghebreab, W., Hauzenberger, C.A., Johnson, P.R., Kusky, T.M., Macey, P., 2013. Orogen styles in the East African Orogen: a review of the Neoproterozoic to Cambrian tectonic evolution. *J. Afr. Earth Sc.* 86, 65–106.
- Ghebreab, W., 1992. The geological evolution of the Adola Precambrian greenstone belt, southern Ethiopia. *Journal of African Earth Sciences (and the Middle East)* 14 (4), 457–469.
- Gichile, S., 1992. Granulites in the Precambrian basement of southern Ethiopia: geochemistry, P–T conditions of metamorphism and tectonic setting. *J. Afr. Earth Sci.* 16, 251–263.
- Johnson, P.R., 2014. An expanding Arabian–Nubian Shield geochronologic and isotopic dataset: defining limits and confirming the tectonic setting of a Neoproterozoic accretionary orogen. *The Open Geology Journal* 8 (1), 3–33.
- Johnson, P.R., Woldehaimanot, B., 2003. Development of the Arabian–Nubian Shield: Perspectives on accretion and deformation in the northern East African Orogen and assembly of Gondwana. In: Yoshida, M., Windley, B.F., Dasgupta, S. (Eds.), *Proterozoic East Gondwana: Supercontinent Assembly and Breakup*, vol. 206. Geological Society, London, pp. 289–325 (Special Publication).
- Kazmin, V., Shiferaw, A., Balcha, T., 1978. The Ethiopian Basement and possible manner of evolution. *Geol Rundsch* 67, 531–546.
- Kroner, A., Stern, R.J., Dawoud, A.S., Compston, W., Reischmann, T., 1987. The Pan– African continental margin in northeastern Africa: evidence from a geochronological study of granulites at Sabaloka. Sudan. *Earth and Planetary Science Letters* 85 (1–3), 91–104.
- Kusky, T.M., Abdel Salam, M.G., Stern, R.J., Tucker, R.D., 2003. Evolution of the East African and related orogens, and the assembly of Gondwana. *Precamb. Res.* 123 (24), 81–85.
- Li, Z.X., Bogdanova, S., Collins, A.S., Davidson, A., De Waele, B., Ernst, R. E., ..., Vernikovsky, V 2008. Assembly, configuration, and break-up history of Rodinia: a synthesis. *Precambrian research*, 160(1–2), 179–210.
- Stern, R.J., 1994. Arc assembly and continental collision in the Neoproterozoic East African Orogen: implications for the consolidation of Gondwanaland. *Annual Review of Earth and Planetary Science* 22, 319–351.
- Stern, R.J., Ali, K.A., Abdelsalam, M.G., Wilde, S.A., Zhou, Q., 2012. U–Pb zircon geochronology of the eastern part of the Southern Ethiopian Shield. *Precamb. Res.* 206, 159–167.
- Teklay, M., Kröner, A., Mezger, K., Oberhänsli, R., 1998. Geochemistry, Pb–Pb single zircon ages and Nd–Sr isotope composition of Precambrian rocks from southern and eastern Ethiopia: implications for crustal evolution in East Africa. *J. Afr. Earth Sc.* 26 (2), 207227.
- Tolessa, S., Bonavia, F.F., Solomon, M., Awoke, H., Eshete, T., 1991. Structural pattern of Pan African rocks around Moyale, southern Ethiopia. *Precambrian Res.* 52, 179–186.

- Tsige, L., 2006. *Metamorphism and gold mineralization of the Kenticha–Katawicha area: Adola belt, southern Ethiopia*. *J. Afr. Earth Sc.* 45 (1), 16–32.
- Tsige, L., Abdelsalam, M.G., 2005. *Neoproterozoic–Early Paleozoic gravitational tectonic collapse in the southern part of the Arabian–Nubian Shield: The Bulbul Belt of southern Ethiopia*. *Precamb. Res.* 138 (3–4), 297–318.
- Verner K., Buri'aneh D., Svojtka M., Peřestý V., Megerssa L., Tadesse T., Kussita A., Alemayehu D., Hroch T.; 2021. *Tectonometamorphic evolution and U–Pb dating of the high–grade Hammar Domain (Southern Ethiopian Shield); implications for the East African Orogeny*. *Precambrian Research* 361 (2021) 106270.
- Woldemichael, B.W., Kimura, J.I., Dunkley, D.J., Tani, K., Ohira, H., 2010. *SHRIMP U–Pb zircon geochronology and Sr–Nd isotopic systematic of the Neoproterozoic Ghimbi Nedjo mafic to intermediate intrusions of Western Ethiopia: a record of passive margin magmatism at 855 Ma?* *Int. J. Earth Sci.* 99 (8), 1773–1790.
- Worku H., Yifa K., 1992. *The tectonic evolution of the Precambrian metamorphic rocks of the Adola Belt (Southern Ethiopia)*. *Ethiopian Institute of Geological Surveys, P.O. Box 2302, Addis Ababa, Ethiopia*. *J. Afr. Earth Sc.* 14 (1–4), 37–55.
- Worku, H., Schandelmeier, H., 1996. *Tectonic evolution of the Neoproterozoic Adola Belt of southern Ethiopia: evidence for a Wilson Cycle process and implications for oblique plate collision*. *Precamb. Res.* 77 (3–4), 179–210.
- Yibas, B., Reimold, W.U., Armstrong, R., Koeberl, C., Anhaeusser, C.R., Phillips, D., 2002. *The tectonostratigraphy, granitoid geochronology and geological evolution of the Precambrian of southern Ethiopia*. *J. Afr. Earth Sc.* 34 (1–2), 57–84.
- Yihunie, T., Adachi, M., Takeuchi, M., 2004. *P–T conditions of metamorphism in the Neoproterozoic rocks of the Negele area, southern Ethiopia*. *Gondwana Res.* 7 (2), 489–500.

Annexes

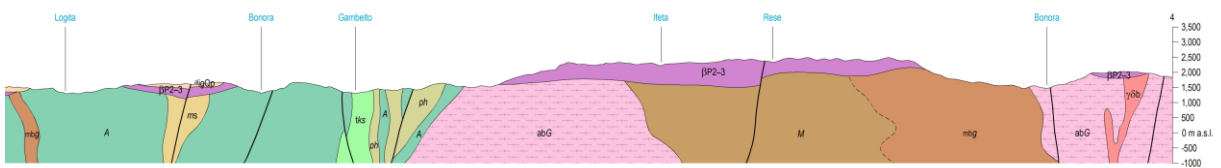
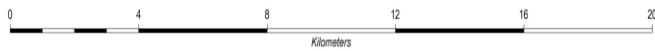
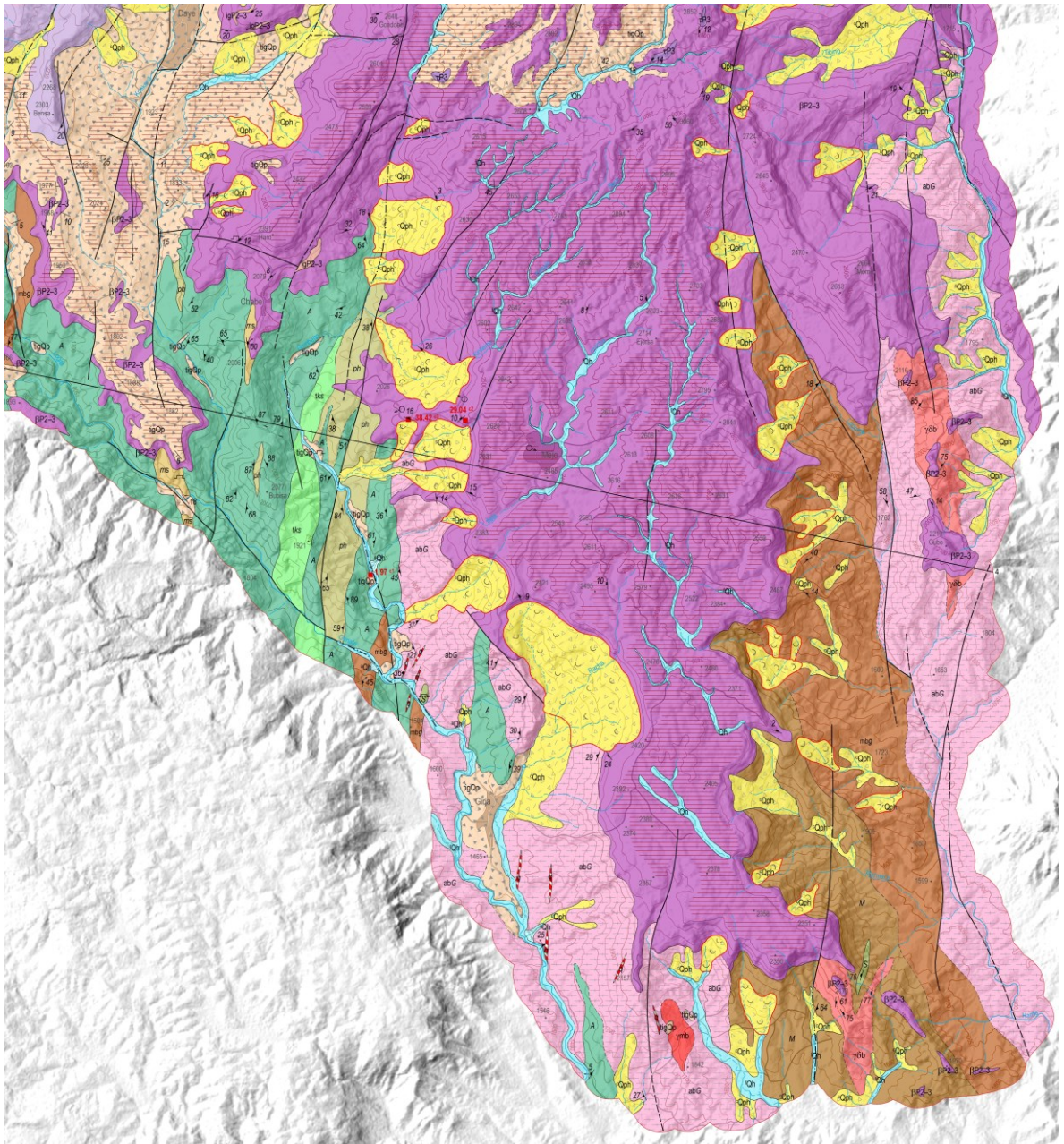
Annex 1. Geological map of Northwestern Hammer Domain (Gamo Zone)



LEGEND

Quaternary Sediments		Miocene		32 MG Igneous and metamorphic rocks assemblage (only in geological cross-section and lithostratigraphic scheme)	
CENOZOIC		15 τN1 Trachyte to trachybasalt		33 ——— Lithological boundary (observed)	
QUATERNARY		106 ρN1 Rhyolite lava with subordinate volcanic breccia and ignimbrite		1000 - - - - Lithological boundary (inferred)	
Holocene		56 βτN1 Alkali basalt to trachybasalt lava and basaltic volcaniclastic deposits		1001 ~~~~~ Significant unconformity (only in lithostratigraphic scheme)	
1 Qh Fluvial sediments		Pre-Rift Volcanic Deposits		35 ——— Fault (observed)	
2 Qh Alluvial fan deposits		PALEOGENE		1002 74 Fault with dip (observed)	
3 Qh Colluvial to alluvial sediments		Oligocene		1003 ——— Fault (inferred)	
4 Qh Lacustrine sediments		18 τP3 Trachyte to trachybasalt lava with subordinate volcaniclastic deposits		1004 ——— Fault (covered by younger deposits)	
5 Qh Lacustrine sediments		57 βτP3 Basalt to trachybasalt		1005 - - - - Mylonitization	
Pleistocene–Holocene		Eocene–Oligocene		40 ——— Mylonitization	
5 Qph Alluvial fan deposits		20 γP2-3 Rhyolite ignimbrite with subordinate rhyolite lava		41 14 Bedding	
6 Qph Colluvial to alluvial sediments		62 βP2-3 Basalt to trachybasalt lava with subordinate basaltic volcaniclastic deposits		42 41 Magmatic foliation	
46 Qph Colluvial to alluvial sediments		21 βP2-3 Basalt to trachybasalt lava with subordinate basaltic volcaniclastic deposits		1009 43 39 Metamorphic foliation	
7 Qph Polygenetic sediments (volcaniclastic, alluvial and lacustrine sediments)		40 βP2-3 Basalt to trachybasalt lava with subordinate basaltic volcaniclastic deposits		1010 44 Volcanic crater	
8 Qph Colluvial sediments		Pre-Rift Sediments		1025 45 Alluvial fan	
Late-Rift Volcanic Deposits		Eocene–Oligocene		1012 46 Landslide	
Upper Pleistocene–Holocene		22 αP2-3 Sandstone		1013 47 Regolith (deeply weathered rock)	
9 ppQph Pumice fall and flow deposits with subordinate polygenetic sediments		101 αP2-3 Sandstone		1015 48 Quarry	
Pleistocene		Southern Ethiopian Shield		1016 49 Spring	
Middle–Upper Pleistocene		NEOPROTEROZOIC		1017 50 Cross-section line	
10 ταQp Trachyandesite to trachyte lava and volcaniclastic deposits		23 Qv Quartz vein		1019 51 2.34 K–Ar dating (Ma – megannum)	
108 ταQp Trachyandesite to trachyte lava and volcaniclastic deposits		64 K Apatite and pegmatite		1020 52 Boundary of mapped area	
Middle Pleistocene		75 K Apatite and pegmatite			
11 βτQp Trachybasalt lava and volcaniclastic deposits		25 γmb Muscovite-biotite granite			
109 βτQp Trachybasalt lava and volcaniclastic deposits		82 γab Biotite and amphibole-biotite granodiorite to tonalite			
Lower–Middle Pleistocene		26 γab Biotite and amphibole-biotite granodiorite to tonalite			
12 βQp Basaltic lava and autoclastic breccia		102 γab Biotite and amphibole-biotite granodiorite to tonalite			
107 βQp Basaltic lava and autoclastic breccia		27 v Amphibole-biotite to amphibole gabbro			
Lower Pleistocene		80 v Amphibole-biotite to amphibole gabbro			
13 βταQp Basalt to basaltic trachyandesite lava and volcaniclastic deposits		66 mbg Biotite to muscovite-biotite paragneiss			
110 βταQp Basalt to basaltic trachyandesite lava and volcaniclastic deposits		28 mbg Biotite to muscovite-biotite paragneiss			
Early-Rift Volcanic Deposits		29 M Migmatite and migmatized biotite paragneiss			
NEOGENE		95 M Migmatite and migmatized biotite paragneiss			
Miocene–Pliocene		30 A Amphibolite			
14 τN Trachyte with subordinate trachyte volcaniclastic deposits		31 abG Biotite to amphibole-biotite orthogneiss			
43 τN Trachyte with subordinate trachyte volcaniclastic deposits		93 abG Biotite to amphibole-biotite orthogneiss			

Annex 2. Geological map of Northeastern Hammer Domain (Sidama Region)



LEGEND

Quaternary sediments		Upper Pleistocene–Middle Pleistocene		Miocene											
CENOZOIC															
QUATERNARY															
Holocene															
1	Qh	Fluvial sediments	11	ipQp	Pyroclastic fall deposits with subordinate rhyolitic ignimbrite	23	pN1	Rhyolite lava with subordinate volcanic breccia and ignimbrite	34	mtg	Biotite to muscovite-biotite paragneiss	48	41	Magmatic foliation	
2	*Qh	Alluvial fan deposits	12	ppQp	Pumice and ash fall deposits	Pre-rift volcanic deposits		35	ms	Sericite schist	49	39	Metamorphic foliation		
3	caQh	Colluvial to alluvial sediments	13	rQp	Rhyolite to trachyle lava	PALEOGENE		36	M	Migmatite and migmatized biotite paragneiss	50	/	Lineation		
4	Qh	Lacustrine sediments	14	igQp	Welded to unwelded rhyolitic ignimbrite with subordinate pyroclastic fall deposits	Oligocene		37	abG	Biotite to amphibole-biotite orthogneiss	51	—	Caldera margin observed		
Pleistocene–Holocene															
5	*Qph	Polygenetic sediments (resedimented pyroclastics, alluvial sediments and lacustrine sediments)	15	iQp	Pyroclastic fall deposits with subordinate ignimbrite	Eocene–Oligocene		38	MG	Igneous and metamorphic rocks assemblage (only in lithostratigraphic scheme and geological cross-section)	52	—	Caldera margin inferred		
6	Qph	Colluvial sediments	Lower Pleistocene		25	igP2-3	Rhyolitic ignimbrite with subordinate rhyolite lava	39	—	Lithological boundary observed	53	⊙	Volcanic crater		
Post-rift volcanic deposits															
7	#pQp	Alkaline basalt lava and basaltic pyroclastic deposits	16	βQp	Transitional alkaline and subalkaline basalt	26	βP2-3	Basalt to trachybasalt lava with subordinate basaltic pyroclastic deposits	40	- - -	Lithological boundary inferred	54	∧	Alluvial fan	
Upper Pleistocene–Holocene															
8	opQp	Obsidian and rhyolite lava	17	*pQp	Alkali rhyolite lava and pumice fall deposits	Southern Ethiopian Shield		41	~~~~~	Significant unconformity (only in lithostratigraphic scheme)	55	⊙	Landslide		
9	ppQp	Pumice fall and flow deposits with subordinate polygenetic sediments	18	igpQp	Rhyolitic ignimbrite and pyroclastic fall deposits	NEOPROTEROZOIC		42	—	Fault observed	56	≡	Regolith (deeply weathered rock)		
Pleistocene															
0	γpQp	Obsidian and rhyolite lava	19	*igQp	Rhyolitic and trachytic ignimbrite	27	▨	Quartz dike	43	—	Fault with dip observed	57	∩	Quarry	
Syn-rift volcanic deposits															
NEOGENE															
Pliocene															
21	βN2	Basalt lava and basaltic pyroclastic deposits	20	igQp	Rhyolitic ignimbrite with subordinate pyroclastic fall deposits	28	γdb	Biotite granulite	44	- - -	Fault inferred	58	○→	Spring	
22	igN2	Welded rhyolitic ignimbrite	NEOGENE		29	γmb	Muscovite-biotite granite	45	· - - ·	Fault obscured	59	●	Thermal Spring		
Pliocene															
23	pN1	Rhyolite lava with subordinate volcanic breccia and ignimbrite	30	S	Serpentinized peridotite and metagabbro	31	tkS	Talc-tremolite and chlorite schist	46	- - -	Mylonitization	60	3-4	Cross-section line	
24	*P3	Trachyle to trachybasalt lava	32	A	Amphibolite	33	ph	Biotite-muscovite phyllite locally with graphite	47	14	∨	Bedding	61	0.451 ±1	K-Ar dating (Ma - megannum)

Annex 3. U/Pb dating result

	CONCORDIA COLUMNS						
file	207/235	7/5 err	206/238	6/8 err	207/206	7/6 err	Rho
DE461-1	1.12605	0.057477	0.128453	0.00649	0.064324	0.003684	0.259662
DE461-2	1.173718	0.052786	0.129256	0.006247	0.066745	0.00357	0.419266
DE461-3	1.16204	0.048879	0.12878	0.006023	0.066173	0.003282	0.352398
DE461-4	1.142521	0.048003	0.128495	0.006225	0.065328	0.003303	0.402738
DE461-5	1.159918	0.053488	0.129289	0.006425	0.065863	0.003534	0.416584
DE461-6	1.305159	0.068394	0.134125	0.00684	0.071598	0.004159	0.258997
DE461-7	1.398711	0.061727	0.147344	0.007149	0.069477	0.003533	0.232439
DE461-8	1.231841	0.063883	0.132664	0.006695	0.068481	0.004143	0.403287
DE461-9	7.570875	0.316357	0.356098	0.017595	0.155257	0.007396	0.274119
DE461-10	5.572935	0.232007	0.260063	0.012864	0.157271	0.007576	0.335551
DE461-11	1.243064	0.086499	0.124955	0.008397	0.073902	0.00577	0.416843
DE461-12	1.160246	0.050074	0.128941	0.006207	0.065865	0.003353	0.369648
DE461-13	1.22154	0.055306	0.132255	0.006351	0.067417	0.003559	0.270279
DE461-14	1.214736	0.052228	0.132621	0.006364	0.066952	0.003425	0.378521
DE461-15	1.162348	0.050142	0.129807	0.006262	0.065434	0.003353	0.386359
DE461-16	1.142362	0.049663	0.125962	0.006002	0.066233	0.003409	0.321457
DE461-17	1.179521	0.060355	0.129905	0.006435	0.066071	0.003801	0.291856
DE461-18	1.168955	0.059705	0.127315	0.006365	0.067632	0.004042	0.425126
DE461-19	1.294098	0.059624	0.143253	0.006971	0.065829	0.003635	0.520361
DE461-20	1.123507	0.049676	0.124864	0.005992	0.06495	0.003314	0.2541
DE461-21	0.463943	0.03866	0.031879	0.002077	0.10958	0.009743	0.295371
DE461-22	1.360353	0.068246	0.138646	0.00697	0.071026	0.004024	0.307897
DE461-23	1.194703	0.057128	0.133291	0.006576	0.064584	0.003405	0.128259
DE461-24	1.184447	0.053281	0.127991	0.006296	0.066463	0.00345	0.346021
DE461-25	1.122484	0.046071	0.127651	0.006082	0.063738	0.003157	0.431147
DE461-26	1.167786	0.054176	0.12768	0.006257	0.066301	0.003579	0.344754
DE461-27	1.144929	0.047956	0.127002	0.006044	0.064973	0.00323	0.355572
DE461-28	1.131101	0.057909	0.126189	0.006435	0.065822	0.003995	0.364627
DE461-29	1.273228	0.060266	0.137178	0.006673	0.066813	0.003577	0.225369
DE461-30	10.5828	0.47557	0.470563	0.024542	0.16337	0.008007	0.220847
DE461-31	1.170276	0.056267	0.129562	0.006382	0.065497	0.003779	0.482552
DE461-32	8.90883	0.363817	0.406046	0.019899	0.158263	0.007531	0.372775
DE461-33	0.643931	0.030271	0.06061	0.003276	0.078521	0.004202	0.443964
DE461-34	1.189766	0.059164	0.132851	0.006663	0.064626	0.003618	0.336624
DE461-35	1.419657	0.064869	0.150258	0.007342	0.068173	0.003554	0.242664
DE461-36	1.227085	0.062526	0.132524	0.006767	0.066382	0.003798	0.368274
DE461-37	1.197495	0.063413	0.128691	0.007078	0.069214	0.004541	0.447894
DE461-38	1.166913	0.051191	0.127609	0.006149	0.065705	0.003359	0.344397
DE461-39	1.156603	0.055027	0.129958	0.006384	0.064314	0.003472	0.294924
DE461-40	1.188236	0.054314	0.129212	0.006141	0.066604	0.003556	0.298104
DE461-41	1.258683	0.060327	0.132271	0.006601	0.068949	0.00372	0.244648

DE461-42	1.107781	0.048744	0.126188	0.006083	0.063586	0.003283	0.279578
DE461-43	1.090959	0.066376	0.111931	0.005901	0.07099	0.00473	0.234818
DE461-44	1.140403	0.050084	0.128106	0.006129	0.06468	0.003369	0.329901
DE461-45	1.129854	0.049099	0.125666	0.005991	0.065119	0.003369	0.378486
DE461-46	1.151832	0.048805	0.128429	0.006161	0.064953	0.003232	0.300412
DE461-47	1.165296	0.055481	0.129617	0.006256	0.06496	0.003583	0.383859
DE461-48	0.699552	0.032552	0.06833	0.003751	0.075139	0.00402	0.513864
DE461-49	1.141901	0.053795	0.128321	0.006258	0.06473	0.003608	0.380616
DE461-50	1.177473	0.056263	0.12918	0.00643	0.065996	0.003562	0.287688
DE461-51	1.165247	0.05529	0.127903	0.006264	0.066068	0.003627	0.377638
DE461-52	0.559063	0.024912	0.035745	0.001907	0.114677	0.00615	0.622508
DE461-53	1.437587	0.062752	0.150008	0.00737	0.069498	0.003553	0.324519
DE461-54	1.017711	0.047357	0.116673	0.005663	0.063562	0.003434	0.264125
DE461-55	1.154641	0.048654	0.129403	0.006161	0.064451	0.003256	0.369191
DE461-56	1.339324	0.056277	0.144134	0.00689	0.06745	0.003402	0.397099
DE461-57	1.125686	0.046755	0.127249	0.006044	0.063682	0.003135	0.342245
DE461-58	0.37264	0.017328	0.026593	0.001363	0.10341	0.005884	0.524376
DE461-59	1.166022	0.061014	0.126612	0.006196	0.066583	0.003915	0.234508
DE461-60	1.174263	0.058968	0.13288	0.006584	0.063013	0.003494	0.247999
DE461-61	0.656179	0.056505	0.032737	0.002296	0.147968	0.012148	0.205094
DE461-62	1.194466	0.061474	0.131279	0.006567	0.066201	0.003863	0.291039
DE461-63	12.43031	0.639539	0.510417	0.029937	0.176993	0.009017	0.33255
DE461-64	1.144507	0.060809	0.126624	0.006375	0.065595	0.003984	0.364864
DE461-65	1.117832	0.05252	0.129075	0.006308	0.062519	0.003366	0.328331
DE461-66	1.170219	0.051511	0.130081	0.006313	0.065314	0.003334	0.354238
DE461-67	1.125133	0.053292	0.124799	0.00599	0.065123	0.00354	0.259367
DE461-68	1.161381	0.052329	0.12906	0.006205	0.06453	0.003305	0.22378
DE461-69	1.167565	0.051173	0.128244	0.006322	0.066054	0.003443	0.460181
DE461-70	1.300904	0.070266	0.142539	0.007201	0.066271	0.003869	0.126496
DE461-71	9.665125	0.466087	0.435126	0.022684	0.160281	0.008675	0.347648
DE461-72	1.106517	0.04981	0.125361	0.006056	0.063259	0.003376	0.453923
DE461-73	1.172937	0.051897	0.133713	0.006455	0.063035	0.003257	0.371392
DE461-74	1.237482	0.053333	0.134229	0.006521	0.065899	0.003346	0.378899
DE461-75	1.162419	0.049913	0.129173	0.006177	0.064401	0.003287	0.417217
DE461-76	8.31036	0.337588	0.380724	0.018549	0.156196	0.007545	0.460834
DE461-77	1.143838	0.051981	0.125994	0.006204	0.064849	0.003486	0.353994
DE461-78	0.376484	0.017656	0.024561	0.001284	0.109402	0.005615	0.286558
DE461-79	1.315265	0.061248	0.141112	0.007061	0.067051	0.003688	0.424299
DE461-80	1.110582	0.047923	0.126414	0.006051	0.063038	0.003247	0.446845
DE461-81	1.134136	0.057057	0.123436	0.006048	0.065621	0.003749	0.226307
DE461-82	1.158222	0.058931	0.131324	0.006515	0.062975	0.003639	0.313284
DE461-83	1.622556	0.08644	0.164008	0.008345	0.07137	0.004364	0.308786
DE461-84	1.119527	0.051585	0.107782	0.005363	0.074001	0.003801	0.137022
DE461-85	1.138592	0.052507	0.126987	0.006095	0.064391	0.00342	0.222913
DE461-86	1.126412	0.049383	0.128729	0.00619	0.063161	0.003309	0.362883

DE461-87	1.141812	0.056872	0.123879	0.006251	0.065744	0.003778	0.390615
DE461-88	1.126691	0.058806	0.124418	0.006098	0.06452	0.003901	0.447063
DE461-89	1.146604	0.049005	0.125841	0.005993	0.06445	0.003272	0.364219
DE461-90	1.110872	0.051028	0.126269	0.006168	0.062678	0.003326	0.206621
DE461-91	1.111379	0.052725	0.123338	0.005997	0.063869	0.003458	0.213167
DE461-92	1.118133	0.052533	0.125528	0.006079	0.062962	0.003416	0.346357
DE461-93	1.150656	0.049535	0.128517	0.006157	0.063839	0.003305	0.352535
DE461-94	1.173483	0.057163	0.129448	0.006292	0.064903	0.003635	0.249682
DE461-95	10.84583	0.479055	0.471064	0.024214	0.163801	0.008333	0.488539
DE461-96	1.209193	0.054698	0.131824	0.006501	0.065125	0.003415	0.328127
DE461-97	1.182134	0.049223	0.130182	0.006239	0.064326	0.003185	0.354507
DE461-98	1.118279	0.050628	0.124728	0.005942	0.063151	0.00336	0.411845
DE461-99	0.566297	0.026944	0.046022	0.002376	0.087708	0.004674	0.296316
DE461-100	9.8352	0.426255	0.433074	0.021233	0.160872	0.007852	0.108322
DE461-101	1.152651	0.052344	0.12513	0.006033	0.065155	0.003457	0.357559
DE461-102	1.213837	0.059713	0.128781	0.006425	0.067101	0.003791	0.362742
DE461-103	1.129469	0.052805	0.127592	0.006247	0.062972	0.003407	0.257658
DE461-104	1.178013	0.052272	0.13265	0.006595	0.063342	0.003394	0.464259
DE461-105	1.131485	0.053972	0.124142	0.006105	0.064743	0.003571	0.376825

file	AGES Ma						Concentrations			U/Th
	7/5 age	2 sigma	6/8 age	2 sigma	7/6 age	2 sigma	U (ppm)	Th (ppm)	Pb (ppm)	
DE461-1	762,2	27,0	778,4	37,0	709	128	231	70	26	3
DE461-2	786,5	24,2	783,3	35,6	806	107	286	101	39	3
DE461-3	780,3	22,9	781,7	35,2	788	104	407	218	81	2
DE461-4	771,1	22,9	779,0	35,5	764	111	409	137	49	3
DE461-5	778,7	25,6	783,1	36,6	770	117	192	60	24	3
DE461-6	842,8	29,8	810,8	38,8	944	115	424	395	158	1
DE461-7	884,5	26,2	885,5	40,1	891	104	329	280	123	1
DE461-8	811,0	29,4	802,6	38,1	837	130	266	146	55	2
DE461-9	2178,8	36,8	1960,3	83,7	2399	81	370	122	124	3
DE461-10	1907,8	36,7	1488,1	65,8	2419	80	572	158	115	3
DE461-11	813,8	39,7	757,9	47,7	975	162	188	102	39	2
DE461-12	778,9	23,3	781,4	35,4	769	109	338	118	44	3
DE461-13	805,9	25,7	800,3	36,2	812	114	299	300	116	1
DE461-14	805,5	23,6	802,4	36,2	809	104	297	626	229	0
DE461-15	779,9	23,3	786,3	35,7	754	108	282	124	45	2
DE461-16	771,7	23,8	764,5	34,3	783	111	320	114	41	3
DE461-17	785,4	27,8	786,9	36,7	775	119	195	79	31	2
DE461-18	784,2	29,2	771,9	36,3	799	130	212	81	30	2
DE461-19	837,7	26,3	862,4	39,3	786	118	232	141	57	2
DE461-20	762,6	23,0	758,1	34,3	760	109	347	138	50	2
DE461-21	377,0	26,6	202,0	13,0	1532	191	81	14	6	6

DE461-22	868,5	29,5	836,6	39,4	929	119	326	98	42	3
DE461-23	790,8	26,4	805,8	37,3	722	115	273	81	32	3
DE461-24	791,6	25,9	775,8	36,0	801	109	282	102	42	3
DE461-25	763,3	22,4	774,1	34,7	714	104	549	201	72	3
DE461-26	781,8	25,3	774,2	35,7	785	111	243	109	40	2
DE461-27	774,8	22,7	770,4	34,5	756	113	461	161	58	3
DE461-28	762,6	27,5	765,4	36,8	753	128	156	51	18	3
DE461-29	830,3	27,0	828,4	37,8	811	117	439	315	121	1
DE461-30	2484,1	44,0	2481,1	106,6	2483	83	307	177	240	2
DE461-31	784,4	26,9	784,9	36,4	742	123	265	91	32	3
DE461-32	2324,1	37,6	2193,8	91,2	2432	84	731	93	109	8
DE461-33	503,1	18,9	378,9	19,9	1113	110	573	134	45	4
DE461-34	791,6	27,2	805,9	36,4	742	119	382	170	63	2
DE461-35	895,3	27,3	901,7	41,1	844	114	230	174	73	1
DE461-36	803,5	28,8	801,1	38,5	765	126	164	49	19	3
DE461-37	799,7	31,3	779,7	40,3	851	129	291	655	117	1
DE461-38	781,6	23,9	773,8	35,1	780	104	341	133	50	3
DE461-39	774,5	25,6	787,0	36,4	726	113	265	92	35	3
DE461-40	790,3	25,2	783,1	35,1	784	111	277	105	40	3
DE461-41	823,8	27,2	800,4	37,6	879	110	468	104	45	4
DE461-42	754,4	23,6	765,8	34,8	705	114	363	140	48	3
DE461-43	745,0	31,4	683,4	34,2	908	135	181	45	20	4
DE461-44	769,1	23,9	776,7	35,0	728	111	260	79	29	3
DE461-45	764,4	23,2	762,8	34,3	751	110	406	154	54	3
DE461-46	776,7	23,5	778,5	35,1	751	108	466	154	56	3
DE461-47	780,2	26,6	785,2	35,6	738	122	173	56	21	3
DE461-48	536,8	19,6	427,0	23,1	1031	110	698	146	48	5
DE461-49	769,9	25,1	779,1	36,6	707	120	256	74	26	3
DE461-50	785,6	26,3	782,7	36,7	772	120	233	88	33	3
DE461-51	780,6	25,3	775,3	35,9	760	121	210	86	31	3
DE461-52	450,2	15,8	226,3	11,9	1846	98	932	235	105	4
DE461-53	901,9	26,8	900,2	41,2	880	108	377	332	147	1
DE461-54	709,6	24,6	711,0	32,6	692	115	204	45	18	5
DE461-55	776,8	23,0	784,2	35,1	738	104	403	153	56	3
DE461-56	861,2	24,9	867,6	38,8	822	107	399	112	46	4
DE461-57	763,5	22,2	771,9	34,5	717	108	516	205	75	3
DE461-58	322,2	13,4	169,1	8,6	1626	106	522	168	40	3
DE461-59	775,4	29,1	768,0	35,5	736	135	148	58	21	3
DE461-60	784,9	27,6	803,9	37,3	697	129	239	87	35	3
DE461-61	491,1	33,8	207,2	14,3	2163	156	101	19	16	5
DE461-62	792,3	28,4	794,6	37,4	778	116	288	104	42	3
DE461-63	2629,7	48,7	2651,5	127,8	2618	84	662	393	545	2
DE461-64	768,8	29,0	768,1	36,5	725	139	230	85	31	2
DE461-65	759,1	25,6	782,1	36,0	668	120	228	69	26	3

DE461-66	783,0	24,0	787,8	36,0	763	104	356	170	61	2
DE461-67	759,8	25,6	757,8	34,3	725	122	208	82	27	3
DE461-68	781,4	24,5	783,3	36,3	741	111	322	110	42	3
DE461-69	783,2	24,7	777,2	36,2	787	111	325	116	45	3
DE461-70	839,8	31,9	858,0	40,6	743	128	123	34	16	4
DE461-71	2385,7	44,1	2320,7	100,2	2425	91	36	21	24	2
DE461-72	752,4	24,0	760,9	34,7	681	125	244	82	31	3
DE461-73	784,1	24,3	808,6	36,7	681	116	314	98	38	3
DE461-74	814,3	24,6	811,4	37,0	787	110	355	367	145	1
DE461-75	781,3	23,0	782,8	35,2	731	110	409	233	87	2
DE461-76	2260,5	36,6	2076,7	86,2	2404	82	417	80	91	6
DE461-77	769,8	24,6	765,9	36,4	715	119	346	122	53	3
DE461-78	323,0	13,0	156,8	8,3	1772	94	1490	189	137	8
DE461-79	849,4	26,7	850,5	39,9	808	116	350	248	96	1
DE461-80	756,7	23,5	767,0	34,7	679	109	386	144	53	3
DE461-81	766,5	26,2	749,8	34,7	746	116	187	47	19	4
DE461-82	773,1	27,8	794,7	37,1	658	128	160	49	19	3
DE461-83	977,6	34,9	979,9	45,0	915	132	110	68	34	2
DE461-84	757,9	24,9	659,3	31,1	1019	102	532	233	64	2
DE461-85	770,5	24,5	770,3	34,8	706	114	296	94	34	3
DE461-86	768,4	24,7	780,2	35,3	670	113	324	140	50	3
DE461-87	766,0	27,3	752,1	35,8	746	121	217	96	37	2
DE461-88	757,5	28,1	755,4	34,9	680	133	167	66	23	3
DE461-89	774,0	23,7	763,8	34,3	729	113	472	179	65	3
DE461-90	755,6	24,5	766,0	35,3	664	120	301	108	39	3
DE461-91	753,2	25,6	749,3	34,4	680	120	227	79	29	3
DE461-92	756,8	25,2	761,9	34,8	682	121	243	80	28	3
DE461-93	774,5	23,2	779,0	35,1	702	116	389	175	62	3
DE461-94	787,5	26,3	784,2	35,8	728	115	217	60	25	4
DE461-95	2505,7	40,5	2485,0	106,2	2486	85	330	269	376	1
DE461-96	801,8	24,9	797,6	36,9	747	112	305	100	41	3
DE461-97	792,3	23,9	788,5	35,6	732	108	555	197	74	3
DE461-98	757,8	24,3	757,4	34,0	682	121	352	111	39	3
DE461-99	454,2	17,8	289,9	14,6	1344	105	689	254	61	3
DE461-100	2412,0	41,6	2315,6	95,8	2451	84	133	94	111	1
DE461-101	774,0	24,7	759,6	34,5	730	118	231	78	28	3
DE461-102	802,3	27,7	780,4	36,6	815	117	303	128	54	2
DE461-103	765,5	25,5	773,6	35,7	657	119	285	111	41	3
DE461-104	786,3	24,8	803,9	38,4	685	117	314	121	48	3
DE461-105	762,8	25,4	753,8	35,0	726	115	213	80	30	3